FLAT OR LUMPY:
SURFACE STRUCTURE AND GROWTH MODES IN SILICON-GERMANIUM EPITAXY

By

ALLISON ARTHUR BAILES III

A DISSERTATION PRESENTED TO THE GRADUATE SCHOOL
OF THE UNIVERSITY OF FLORIDA IN PARTIAL FULFILLMENT
OF THE REQUIREMENTS FOR THE DEGREE OF
DOCTOR OF PHILOSOPHY

UNIVERSITY OF FLORIDA

1998

"God created the bulk. The devil created surfaces."

Anonymous

ACKNOWLEDGMENTS

Liz Seiberling, my advisor for these past five years, deserves tremendous credit for my reaching this stage of my graduate career. Not only has she put up with me all this time, but she also has provided an environment in which I have been able to flourish in the good times and survive in the bad times. She has always rendered just the right kind of support to keep me on the path, whether that was a warning to shape up or succor when I wanted to quit. For her patience with me as I plodded along and for her friendship, I am eternally grateful.

Mark Boshart, one of the first students I met when I arrived in 1991, was a friend and study partner as I struggled through the core courses in the first year. We continued working together when I joined this research group, and he taught me much that I know about transmission ion channeling. The many hours that we spent together in the lab—preparing samples, taking data, inventing games—were an important part of my time here. From Mark Grant I learned the delicate art of transferring samples between our ultra-high vacuum chambers and other important lab skills. We also enjoyed many Saturday mornings of playing basketball together at the Hume courts.

Roland Johns, Bob Litwins, the late Donny McNeill, and Ivan Kravchenko served excellently in running the Van de Graaff accelerator and helping with experimental problems related to the accelerator. Ivan also was of great help as I traced electronic problems in our data acquisition system. Bill Malphurs, Ed Storch, and Bobby Fowler in the machine shop always came through for me when I brought them a job with little or no lead time. Gene Dunnam and Henri Van Rinsvelt have been helpful and willing to impart to me their vast knowledge of the accelerator whenever asked and both aided me in my job search.

As everyone in the physics department must be aware, Joan Raudenbush is the person to see when you need a straight answer about the inner workings of the department bureaucracy. She has rescued me numerous times when others obfuscated. Not only has she done the jobs of two people most of the time that I have been here, but she has always done them with alacrity. She is also a just plain nice person with whom I have enjoyed occasional chats throughout my time here. Cindy Bright, Janet Germany, Darlene Latimer, and Susan Rizzo have also proved invaluable in my dealings with purchases, paperwork, and packages. Chandra Chegireddy and Dan Roscigno have set the standard for computer support so high that I am afraid of what I may find in other places when I move on.

Herbert Dacosta, who just defended his second Ph.D., has been an inspiration to me as well as a great friend and Portuguese tutor. Bruce Paul and I, having both started at UF in 1991, spent many hours studying together in the early days. We also enjoyed, with John Canellos and Morten Hallgren, a memorable evening of trying to forget our first bout with the comprehensive exams as we drank too many pitchers of beer at the Market Street Pub. As a study partner and lunch companion, Servio Medina helped make the early years bearable, and Steve “I’ll bring Jackson” Thomas helped to make the later years possible as we worked many problems together in the summer of 1993 to prepare for my second bout with the comprehensive exams. Others who have passed through our research group and deserve mention for their friendship are Bas Feddes, Greg Martin, Micah Ohalloran, Rick Piciullo, and Mel Pfautz.

Whereas the above-mentioned people all helped me to survive graduate school, Donald Ryan, Isaac Asimov, Jeff Trahan, Gary Hallee and Doug Caulkins were crucial to my being here in the first place. Dr. Ryan, a mathematics professor at Northwestern State University in Natchitoches, Louisiana, ran a summer academic program which fueled my desire to pursue an academic career. The book *Asimov on Physics* is fully responsible for that career being in physics rather than chemistry, and Jeff Trahan and Gary Hallee, my two undergraduate physics professors, validated my decision by making me love physics. Doug Caulkins, a good friend during my undergraduate days, inspired me with his intelligence and creativity and showed me a whole new way of looking at the world.

Of course, my family deserves special mention for helping me to become who I am. My mother and father have always encouraged my academic interests and helped me in countless other ways. My paternal grandparents, Mam-maw and Pap-paw, provided total support and love and inspired my imagination by having a home with a wonderful array of old junk and woods with a creek. My sisters Ann, Catherine, and Suzanne have been an important part of my life, and my Aunt Verla helped make this degree possible by her financial support of my undergraduate education.

Other friends who have made my stay in Gainesville a pleasant and interesting one are Randy Cullom, Bill Stephenson, and Zot Szurgot. Randy is the guy you always want on a camping trip because if you have forgotten something, he has it. He also makes a great “sammich.” Bill and Zot brightened the past three years immeasurably by inviting me and my wife to live with them on Newnans Lake, where they were always fun to live with and a big part of the great parties we have had there.

Some important miscellany that have helped with my peace of mind during this crazy time are my dog Calli, my kitties Malva and Circe, *The Funny Times,* Newnans Lake, Ocala National Forest, the Marx Brothers, Payne's Prairie, Lachua trail, Enya, Zippy the Pinhead, Edward Gorey, REM, J. R. R. Tolkein, Burrito Brothers, Leonardo's, Ben & Jerry, and lastly, the hours between midnight and 6 am, when most of this dissertation was written.

Finally, my wife Myra deserves more praise than words can express, for I have difficulty imagining what these seven years of graduate school might have been like without her love and support. Through all the good times and the bad times, she has been the one person on whom I could depend for total, unconditional support. From the beginning, she has accepted with uncommon poise all of the hardships that a spouse in graduate school can place on a marriage.

TABLE OF CONTENTS

page

ACKNOWLEDGMENTS iii

ABSTRACT ix

CHAPTERS

1 INTRODUCTION 1

2 EXPERIMENTAL SETUP AND SAMPLE PREPARATION 7

Sample Preparation 7
Ion Beam Production 10
Beam-Sample Interaction 11

3 TECHNIQUES FOR DETERMINING SURFACE STRUCTURE 16

Low Energy Electron Diffraction 16
Transmission Ion Channeling 18
  Ion Channeling 20
  Ion Scattering 24

4 DATA COLLECTION AND ANALYSIS 28

Data Collection 28
Data Analysis 32
  Preliminary Analysis 32
  Angular Scans and the Continuum Approximation 36
  Energy Distributions and the Monte Carlo Simulation of Channeling 39

5 SURFACE STRUCTURE DURING SURFACTANT-MEDIATED EPITAXIAL GROWTH OF GE ON SI(100) 65

Background 65
  The Si(100) Surface and Epitaxial Growth 66
  Surfactant-Mediated Epitaxy 70

Experiment 80
Results and Discussion 83
The Single-Adatom Exchange Model and Previous Data 83
High Ge Coverage 90
Intermediate Ge Coverage and Incremental Annealing 96
Summary 114

6 DIMER ELONGATION ON THE MONOHYDRIDE-COVERED GE/SI(100) SURFACE 116

Background 116
Experiment 118
Results and Discussion 120
Ge Dimer Geometry 120
Hydrogen Recoil Data 126
Summary 128

7 CONCLUSION 130

REFERENCES 133

BIOGRAPHICAL SKETCH 140

Abstract of Dissertation Presented to the Graduate School
of the University of Florida in Partial Fulfillment of the
Requirements for the Degree of Doctor of Philosophy

FLAT OR LUMPY:
SURFACE STRUCTURE AND GROWTH MODES IN SILICON-GERMANIUM EPITAXY

By

Allison Arthur Bailes III

August 1998

Chair: Lucy Elizabeth Seiberling
Major Department: Physics

We have investigated the surface structure of Ge/Sb/Si(100) and H/Ge/Si(100) with transmission ion channeling. The former was a continuation of our studies of surfactant-mediated epitaxy and our attempt to determine the exchange mechanism as the surfactant segregates to the surface during growth. The method of analysis used for this part was comparison of experimental with simulated scattered ion energy distributions. Our interest in the latter system grew out of the differences observed between H/Si(100) and H/Ge(100). We studied this system using the traditional angular scan (yield versus tilt) analysis.

After depositing Ge on Sb-terminated Si(100)-2x1 at room temperature (RT), we collected ion scattering data near the <100> direction of beam incidence. First, we determined that the single adatom exchange model did not fit our previous data for Ge

coverages of 0.15 ML and 0.68 ML. Second, we deposited 2 ML Ge and found the system at RT to be in the same configuration that we had found for 0.68 ML Ge (elongated Ge dimers). Third, we studied this system with 0.4 ML Ge after RT and after anneals at 80° C, 150° C, 200° C, 350° C, and 500° C. We found the Ge to be described by the all dimer model at RT and 80° C, an intermediate state at 150° C and 200° C, and the final state (Sb dimers and near-substitutional Ge) at 350° C, and 500° C. We also were able to rule out certain exchange models proposed in the literature.

We had difficulty determining which of three configurations best described the Sb structure in this experiment because of limitations in the method of analyzing energy distributions. We found energy shifts in the experimental distributions that can be caused by thickness variation and perhaps by deformation of the sample because of strain in the Ge layer.

Finally, in our study of the monohydride-covered Ge/Si(100) surface, we determined that the Ge dimers were elongated relative to the previously studied Ge/Si(100) without H. The dimer bond length was 2.8 Å and the dimers were untilted, whereas previous work found that the bond length is 2.6 Å and the tilt is 12° for Ge/Si(100) without H.

CHAPTER 1
INTRODUCTION

When so much has been done already to understand the Si-Ge system, why should we pursue further studies in this area? The overriding answer, of course, is that Si is the backbone of the microelectronics industry and is likely to maintain that role. For that reason, any new knowledge is potentially useful, if not directly then perhaps as a guide to new studies.

As the density of functions of a Si chip increases, the traditional electronic interconnects within the chip become the limiting factor to further improvement. Electronic interconnects dissipate too much heat for a high density chip to handle, and these interconnects cannot operate at the required frequencies of 500 MHz and higher [Fit98]. An important technological goal then is to replace the electronic inter- and intra-chip connections with optical links, thereby achieving the integration of photonics and electronics. As testament to the value of this line of research, the April 1998 issue of the *MRS Bulletin* was devoted entirely to Si-based optoelectronics.

Although compound III-V semiconductors emit light more easily, our current technology is based on Si. Thus, the effort to create light-emitting Si devices has gained momentum with increasing chip density. One way to accomplish this feat is by fabricating superlattices, alternating layers of different materials separated by abrupt, flat interfaces (Figure 1-1). Through variation of the layer thickness, the electronic properties of the resulting device can be manipulated. With Si-Ge superlattices, the goal is to create a device that has a direct bandgap and will emit light [Pre92].

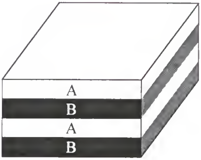

Figure 1-1. Multilayered superlattice.

Rough interfaces diminish the quality of the desired electronic properties, but they are the normal result of epitaxial growth of these structures. Because of thermodynamic restrictions, if material A grows flat on material B, then B will be lumpy when grown on A. Furthermore, even if A initially grows layer by layer, many materials eventually start forming three dimensional islands on the surface. This lumpy growth can be mitigated by reducing the sample temperature during growth or increasing the growth rate. Both of these means, however, reduce the quality of the film.

With the introduction of a small amount of a third material of the proper type, the growth modes can change from lumpy to flat. This method is called surfactant-mediated epitaxy (SME) and has been studied with a wide range of materials. (A detailed review of the literature for this method is given in Chapter 5.) Our interest in this method is to learn about the exchange mechanism involved in the segregation of the surfactant (Sb in our experiments) to the surface when the film material (Ge) is deposited on top.

Aside from the importance to the electronics industry, SME still poses some intriguing questions that as yet have not been answered convincingly. For example, why does SME change the growth mode? Are the causes of the change in growth mode thermodynamic or kinetic in origin? Is reduced diffusion of adatoms on the surface necessary for layer by layer growth to occur? Do Sb and As as surfactants indeed reduce the diffusion of adatoms, as many suggest, or do they enhance diffusion?

The question that we have focused on in our work in SME is the nature of the exchange mechanism (Chapter 5). Three models have been proposed to explain the exchange process, and we have performed experimental studies to look for evidence that would support or contradict these models. All of the models suggest different surface structures as the system goes from the symmetric Sb dimers on the Si(100) surface before Ge deposition to asymmetric Sb dimers on near-substitutional Ge on Si(100) after the exchange has occurred. The initial and intermediate stages of all three models have Ge in dimer sites, but the Sb sites differ dramatically. Two models posit different amounts of substitutional Sb sites whereas the other suggests Sb in near-interstitial sites.

Our effort to understand this exchange process and which, if any, of the theoretical models is best described by experimental data began with the work published in Mark Boshart's Ph.D. dissertation [Bos96a] and in Boshart *et al.* [Bos96b]. That work studied the Ge/Sb/Si(100) surface structure after 0.15 ML and 0.68 ML Ge had been deposited at room temperature (RT) and then annealed at 350° C. What we found was that the low Ge coverage revealed little other than that the Sb was still in dimer sites before and after annealing. At the higher Ge coverage, however, we found the Ge to be in dimer-like sites and the Sb to be undisturbed by the Ge adsorption (i.e., in symmetric dimer sites) before annealing. Upon annealing, we found the system to be in the final state, that is, with Ge in near-substitutional sites and Sb in asymmetric dimer sites. We used those data to test two of the models that had been proposed and found one not to fit our data at all and a modified version of the other to fit the higher Ge coverage data before annealing. We called this modified version the all dimer model.

This was a good beginning, but we had neither convincingly eliminated one of the models nor clearly identified the initial state of the exchange process. We had a result based on limited data, and perhaps changing the Ge coverage or annealing at other temperatures would reveal a completely different surface structure. As will be discussed in Chapter 5, the Ge coverage of 0.68 ML is not the ideal coverage for testing the validity of the exchange models because ~0.4 ML saturates the surface for most of the atomic configurations that we tested. In addition, another model had been proposed since that early work was published. Thus, the SME results presented in this dissertation comprise (i) testing the new model against the previous data, (ii) studying the system at a Ge coverage of 2 ML, and (iii) testing the models at 0.4 ML Ge and at several different temperatures.

By monitoring the surface structure for different amounts of Ge deposited at RT on the Sb-terminated Si(100)-2x1 surface and then annealed at several different temperatures from 80° C to 500° C, we have attempted to follow the segregation path. We found that the Ge starts out in elongated-dimer sites at RT (the all dimer model), goes through an intermediate state at about 200° C, and then reaches near-substitutional sites between 350° C and 500° C. Also, the initial Ge site of elongated dimers remains the same whether the coverage is 0.4 ML or 2 ML. Regarding the Sb positions during segregation, we clearly did not see evidence of substitutional Sb or of a large amount of interstitial Sb. We came across unexpected problems with our method of analysis, however, when it came to distinguishing between configurations that had Sb in different dimer sites and with the possibility of some near-interstitial dimers.

The experimental technique we used to study this system is transmission ion channeling (Chapter 3). We collected scattered ion energy distributions for directions of beam incidence near the <100> axis and compared these distributions to simulated energy distributions obtained from a Monte Carlo simulation of the ion channeling process (Chapter 4). Ideally the comparison is based on peak height, shape, and position on the energy axis. What we found, however, is that we often have enhanced ion energy loss in the axial and occasionally in the planar directions, making energy comparisons difficult. Some of this energy loss may be due to thickness variation, but apparently another mechanism is involved as well. One possible explanation is that the strain in the Ge layer causes deformation of the crystal.

In addition, we have studied the monohydride-covered Ge/Si(100) system (Chapter 6). Although H also has been shown to act as a surfactant, our study of this system is not directly related to SME. Rather, we began out of an interest in the structural differences manifested in the H/Si(100) and H/Ge(100) systems, and we also desired to learn about the effect that H has on the Ge layer. For Ge/Si(100) without H, previous work has found that the Ge adatoms are in asymmetric dimer sites with a dimer bond length of 2.6 Å and are tilted at 12° relative to the (001) surface plane [Gra94c]. We found that in the H/Ge/Si(100) system, the Ge dimers are longer (2.8 Å) than the dimers in Ge/Si(100) without H and also are not tilted, in contrast to the Ge/Si(100) dimers. The

---

analysis in this study was based on a comparison of experimental and calculated angular scans (Chapter 4) taken near the <100> and <110> beam incidence directions. Our original intention was to determine the H sites also, but this proved impossible because of an inability to distinguish between H on the front and back of the sample and because of poor statistics in the H peak.

CHAPTER 2
EXPERIMENTAL SETUP AND SAMPLE PREPARATION

To study semiconductor surface structure with ion beams, one needs ultrahigh vacuum (UHV) chambers for preparing contaminant-free samples, a source of ions, and a means of delivering the ion beam to the sample in the UHV environment. Each of these three requirements entails the use of complex and interconnected equipment. For the experiments reported here, this equipment is in the Van de Graaff accelerator laboratory at the University of Florida. Because the Ph.D. dissertations of Paul Lyman [Lym91a] and Mark Grant [Gra94a] provide detailed descriptions of the laboratory, only a brief overview will be given here.

Sample Preparation

The first stages of sample preparation take several days and occur in the chemistry laboratory. Because transmission ion channeling requires samples thin enough for transmission of the beam, the Si, originally ~500 μm thick, must be thinned to ~1 μm (10,000 Å) or less. (Most of the "thin windows" that we make have a thickness between 3000 Å and 6000 Å.) To remove the excess Si, we use a dopant-selective chemical etch, as detailed in the paper by Cheung [Che80]. This procedure begins with a diffusion of boron, which stops the chemical etch, into the polished side of the Si wafer. The B concentration after the diffusion is 4×10^{19} atoms cm^{-3} [Lym91a], high enough to alter the electronic properties of the Si but low enough not to affect the structural properties significantly. The second stage is a fast etch of the masked sample to remove a large amount of the Si in a short time (~20 minutes). The etching solution used here is not sensitive to boron, but the third stage—the slow etch—does stop at the B layer. After the slow etch, the sample consists of a rectangular piece (~15 mm on a side) of Si of the original thickness (~500 μm) with a thin circular window of diameter ~6 mm and thickness ~5000 Å (Figure 2-1). Although samples generally vary in thickness by only ~10%, we occasionally see greater variation, as will be discussed in greater detail in Chapter 4. The final phase of sample preparation in the chemistry laboratory is cleaning the samples and protecting them with an oxide layer (the "Shiraki oxide") using the procedure developed by Ishizaka and Shiraki [Ish86].

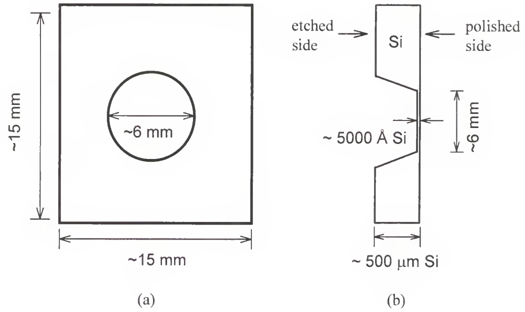

Figure 2-1. Si thin windows after dopant-selective chemical etch. a) Top view; b) side view.

Once the *ex situ* preparation is complete and the samples are mounted on modules, they are placed into the UHV chambers, three interconnected chambers for sample storage (introduction chamber), *in situ* sample preparation (preparation chamber), and ion scattering experiments (scattering chamber). The samples are first put into the introduction chamber on a carousel that holds five modules. The base pressure of this chamber is $2x10^{-9}$ torr, sufficiently low that the preparation chamber pressure degrades only temporarily during sample transfers.

The preparation chamber, with a base pressure of $4x10^{-11}$ torr, is where most of the *in situ* preparation occurs. The first stage in this treatment is desorbing the protective oxide layer by placing the sample (polished side forward) in front of the heat lamp and heating by irradiation to 900° C. As detailed in the Chapter 3, we determine when the Si surface is sufficiently clean by monitoring the low energy electron diffraction (LEED) pattern after each ten to twelve minutes of sample heating. When we attain a two-domain 2x1 pattern that has low background and sharp spots and covers most of the surface, we then deposit adsorbates onto the polished side of the sample. To deposit Sb and Ge, we use boron nitride effusion cells heated to an appropriate temperature for each species (600° C for Sb and 1150° C for Ge). With the sample on the preparation chamber manipulator positioned in front of an effusion cell, opening the cell shutter for a given amount of time controls the amount of material deposited. A Ta heat strip, mounted on the manipulator behind where the sample sits, can provide sample heating by irradiation during the deposition. Calibration curves show the temperature as a function of time and current through the heat strip. The other deposition method available to us is the introduction of gases into the chamber through a leak valve. We deposited atomic hydrogen in this manner by passing molecular hydrogen over a hot filament and filling the chamber to a pressure of 10^{-6} torr. After each stage of adsorbate deposition, the LEED pattern is checked and described in the logbook.

Ion Beam Production

The Van de Graaff accelerator, manufactured by High Voltage Engineering Corporation, can provide beams of $^{1}H^{+}$, $^{4}He^{+}$, $^{4}He^{++}$, $^{3}He^{+}$, or $^{3}He^{++}$ with energies from 500 keV to 3.5 MeV for the singly charged ions or up to 7.0 MeV for the doubly charged ions. The machine ionizes the gases in a region of high electrostatic potential and accelerates them as they move toward ground potential. As they move downward, they also are focused, and the energy is selected by bending the beam 90° through the dipole analyzing magnet. A nuclear magnetic resonance probe in this magnet measures the magnetic field, which determines the energy of the beam, and the electronic circuitry adjusts the magnet current to keep the magnetic field, and thus the beam energy, constant. Just past the analyzing magnet, the beam passes through horizontal and vertical slits, with the energy resolution of the beam determined by the size of the horizontal slit. Another dipole magnet, called the "switching" magnet, then sends the beam into one of five beamlines.

One issue of concern in the area of beam production is beam contaminants, that is, ions other than the intended ones accelerated and bent through the analyzing and switching magnets along with the primary beam. We have seen evidence of $^{16}O^{++}$ in the $^{4}He^{+}$ beam [Bos96c] and $^{1}H_2^{+}$ in the $^{4}He^{++}$ beam. (Since we used only a $^{4}He^{+}$ beam for the work reported here, the latter beam contaminant will not be discussed.) The basic equation that governs the bending of an ion beam through a magnet is

$$r = \frac{\sqrt{2mE}}{qB} . \tag{2-1}$$

Thus, for a given setting of the magnetic field B, any ions with the same $\sqrt{mE}/q$ will pass through the magnet and continue through the beamline together. In the case of $^{16}O^{++}$ and $^{4}He^{+}$, this quantity is not equal for the two different ions. However, when oxygen is accelerated in its singly charged state and stripped of the second electron before entering the analyzing magnet, $\sqrt{mE}/q = \sqrt{10}$ for both beam components.

Experiments with $^{4}He^{+}$ scattering from a thin layer of Au on Si(100) led to the conclusion about oxygen contamination in the $^{4}He^{+}$ beam. Understanding an anomalous peak, whose position in the scattering spectrum did not fit any reasonable sample contaminants, eluded us until Mark Boshart looked into the possibility of beam contamination. (See Appendix A in Boshart's Ph.D. dissertation [Bos96c].) He found an earlier study [Pic73] that explained how the oxygen was created (sputtering in the quartz bottle where the He is ionized and ionization of molecules in the vacuum system) and how it was transmitted along with the helium (stated above). Boshart also estimated, based on the peak areas and cross sections of $^{4}He^{+}$ and $^{16}O^{++}$ scattering off of Au, that the oxygen makes up approximately 0.4% of the incident beam.

Beam-Sample Interaction

After the sample is prepared and the ion beam is ready, the next step is to bring them together. To deliver the beam from the accelerator, which maintains a pressure of

10^{-6} torr, to the scattering chamber, whose base pressure is 4×10^{-11} torr, we use a differentially pumped beamline that has a high resistance to gas flow due to its small diameter tubing and the presence of a liquid nitrogen cold trap. This arrangement allows us to open the UHV chamber to the higher pressure accelerator with only a minimal degradation of the vacuum. We can normally maintain pressures of 1×10^{-10} torr or less with the beam on the sample.

With all the valves open, we align and focus the beam before transferring the sample into the scattering chamber. Small dipole magnets provide steering to keep the beam near the center of the beamline, while a larger quadrupole magnet focuses the beam on the end of the beamline. As will be discussed in Chapter 3, channeling experiments require a small angular divergence of the ion beam entering the crystal. Therefore, we focus the beam on the end of the beamline, 70 cm behind the sample. When the beam is focused and centered, we then reduce the cross sectional area of the beam by placing a plate containing a small aperture across the beamline. This plate is about halfway between the quadrupole focusing magnet and the scattering chamber, and the angular divergence for this setup is 0.03°. Reducing the beam size serves two purposes: limiting the amount of beam current so that crystal damage is minimized and having the beam interact with a smaller area on the sample so that substrate thickness and adsorbate coverage do not vary appreciably.

After aligning and focusing the beam, we then block the beam from entering the scattering chamber while we transfer the sample from the preparation chamber. The module, which holds the sample, is placed onto a two-axis goniometer in the center of the scattering chamber (Figure 2-2) and seated securely. The goniometer can rotate about a

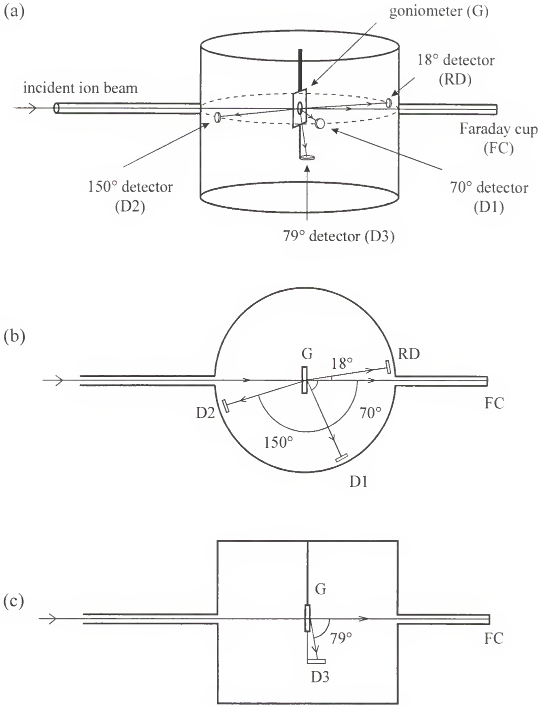

Figure 2-2. Scattering geometry and location of detectors. a) Three dimensional view; b) top view; c) side view.

horizontal axis that is nearly parallel to the sample normal and about a vertical axis. The rotation angle around the vertical axis is referred to as A and about the horizontal axis, C. Because we do not have the capability to rotate about a third axis (perpendicular to the sample normal), the sample module sits in the goniometer with a 5° offset relative to the horizontal axis of rotation. This offset ensures that we can align the beam with the sample normal (the <100> crystal axis). The goniometer also can translate in the x, y, and z directions.

When the beam hits the sample, He^+ ions interact with the Si substrate and with the adsorbates (see Chapter 3 for details). The scattering chamber is equipped with four detectors (Figure 2-2) for analysis of scattered He^+ ions and recoiled H atoms. The detectors at 70°, 79°, and 150° are set up for He^+ ions and the 18° detector, because of its small scattering angle and the Al foil to stop He^+ ions, collects H recoils. The detectors are of the ion-implanted, solid state type [Mod95]. Basically, they are Si diodes operated with a reverse bias voltage to collect the electrons and holes that are created by the passage of a charged particle (He or H). The quantity of electrons and holes collected is a measure of the energy of the incident ion. The collected charge is then converted to a voltage pulse whose height is proportional to the ion energy. The pulse is amplified and then converted to a digital signal that is fed into the multichannel analyzer program on the data acquisition personal computer.

Important to note is that the 79° detector (Figure 2-2(c)) is attached to and rotates with the goniometer. The angle of 79° is the angle between the detector and a horizontal plane that contains the beam, but the scattering angle can differ from 79°. As the goniometer is rotated so that this detector moves out of the vertical plane that contains the beam, the scattering angle becomes greater than 79°. For tilts of 6°, the change in scattering angle is only ~0.1°, but at a tilt of 45° (where the <110> axis is found), the scattering angle increases to ~82°. When the sample is in backscattering geometry (adsorbate-covered surface facing the beam), the scattering angle is 180°-79° = 101°.

CHAPTER 3
TECHNIQUES FOR DETERMINING SURFACE STRUCTURE

The experiments discussed in this work have one aim: determining the arrangement of adatoms on the Si(100) surface. To achieve this aim, we use two complementary techniques. Low energy electron diffraction (LEED) probes the long range order, or periodicity, of the surface layer relative to the underlying substrate. We use this technique after each stage of sample preparation to ascertain that we have the surface periodicity that we want or to monitor changes induced by adsorption or annealing. Transmission ion channeling, our main technique, is sensitive to the short range order and can pinpoint the positions of adatoms relative to the substrate lattice with a typical resolution of better than 0.1 Å.

Low Energy Electron Diffraction

When waves of wavelength λ encounter a periodic array of scattering centers whose spacing is of the order of λ, the scattered waves will interfere, creating a pattern of light and dark areas corresponding to constructive and destructive interference. This property has allowed crystallographers to determine bulk crystal structure by scattering x-rays from crystals and analyzing the resulting diffraction patterns, which are k space representations of the crystal structure. A beam of low energy (~100 eV) electrons also will diffract from a crystal because the electron de Broglie wavelength is of the same order as the interatomic spacing (~1 Å). Davisson and Germer first demonstrated this wave property of electrons in 1927 [Dav27]. The important difference between diffracting x-rays and electrons, however, is the mean free path. X-rays penetrate deeply (~10 μm) without attenuation, whereas diffracted low energy electrons interact only with the surface layers (~10 Å). (Detailed descriptions of LEED can be found in the works by Feldman and Mayer [Fel86], Woodruff and Delchar [Woo94], and Zangwill [Zan88].)

LEED patterns yield important information to the surface scientist. The presence of a pattern with sharp spots indicates that the surface is well-ordered, and the arrangement of diffraction spots shows how the periodicity of the overlayers compares to that of the substrate. The pattern cannot pinpoint atomic positions, however, because surfaces with different atomic configurations may have the same periodicity and hence the same diffraction pattern. An ideal, bulk-terminated (100) surface of a cubic crystal produces the LEED pattern shown in Figure 3-1(a). The designation "1x1" indicates that the period of the overlayer, in both directions of the surface net, is the same as the period of the corresponding plane anywhere in the bulk. In the 2x1 pattern shown above (Figure 3-1(b)), the period of the overlayer is twice that of the ideal surface in one direction and the same as the ideal surface in the other direction. Working backward from the

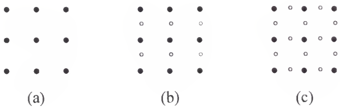

Figure 3-1. Basic LEED patterns. Solid circles are first order spots and open circles are half order spots. a) 1x1; b) 2x1; c) 2x2.

diffraction pattern (the natural order in the lab), we see that these extra, "half order" spots in the LEED pattern imply the doubling of the periodicity in real space.

In the course of our experiments, we employ LEED after each stage of sample preparation: producing the "clean" Si(100) surface, depositing adsorbates on the clean Si(100) surface, and annealing the sample. After each stage, we visually monitor the LEED pattern, noting the type of pattern, the background level, the size of the spots, the relative intensity of the half order spots, and how the pattern changes when the electron beam energy is changed. The first pattern that we see upon removing the protective oxide from the Si(100) sample is the 2x2 pattern shown in Figure 3-1(c). In subsequent chapters, this pattern will be referred to as a two-domain 2x1 pattern because it results from nearly equal contributions of 2x1 and 1x2 domains on the Si(100) surface. These two domains derive from the stepped surface with dimer rows that run perpendicular and parallel to the step edges on alternating terraces. As other species are adsorbed onto the clean Si(100) surface or the sample is annealed, we typically see an increase in the background level and weakening or disappearance of the half order spots.

Transmission Ion Channeling

As a probe of local order, transmission ion channeling provides information that LEED patterns cannot: details of the atomic configuration of the overlayers. The two requirements of this technique are a single crystal thin enough to transmit an ion beam and beam incidence near a major crystallographic (low Miller index) direction. Under these conditions, the ion beam is channeled through the crystal, and the ion flux on the beam exit side of the crystal is no longer uniform. The power of this technique arises from the surface of interest being placed on the beam exit side of the crystal, allowing the adatoms to interact with the non-uniform ion flux. Scattered ions and recoiling adatoms can then be detected with little restriction on the placement of detectors. Figure 3-2 shows a typical setup for a transmission ion channeling experiment.

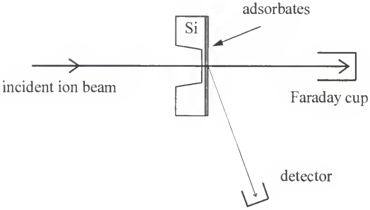

Figure 3-2. Scattering geometry for transmission ion channeling.

As in the case of Rutherford backscattering spectrometry (RBS) [Chu78], transmission ion channeling can be understood by looking at what happens to an ion beam as it passes through a material and how an ion undergoes large-angle scattering. The most important aspect of an ion beam's passage through a material is that it can be channeled for certain alignments of beam and single-crystal sample. Two other transit processes that must be considered are the energy loss of the ions as they interact with sample electrons and energy straggling of the beam due to statistical fluctuations in the energy loss. Detection of scattered ions at angles between 0° and 180° is possible because a small fraction of the ion beam will penetrate closely enough to sample nuclei to undergo elastic, binary collisions. The kinematic factor determines the energy of the scattered ion, and the scattering cross section gives the probability for scattering. All of these processes are important in transmission ion channeling and will be described in greater detail in the following two sections.

Ion Channeling

Channeling occurs when rows or planes of atoms in a crystal steer ions into the open spaces (channels) between the rows or planes. This effect was first predicted by Stark in 1912 [Sta12] but not observed in the laboratory until the 1960s (and then mainly by accident). Anomalously long ranges of ions in solids, observed experimentally [Pie63] and in computer simulations [Rob63], led to the discovery of channeling, and the basic theory was presented by Lindhard in 1965 [Lind65]. Channeling has been observed with positive, neutral, and negative particles in the keV to GeV range and has been used in high energy physics, nuclear physics, atomic physics, and materials analysis. Light, positive ions in the MeV range are our concern, and general references on their use in materials analysis are the book by Feldman, Mayer, and Picraux [Fel82] and *Handbook of Modern Ion Beam Materials Analysis* [Tes95].

A uniform ion beam incident on a thin crystal in a direction that is not aligned with crystallographic axes or planes still will have a uniform flux distribution as it exits from the material (Figure 3-3(a)). The crystal in this alignment has the same effect on the beam as an amorphous solid, whose constituent atoms are arranged randomly. This alignment, thus, is called “random”. On the other hand, when a uniform ion beam enters a thin single crystal near a low index direction, the ions are steered through channels in the crystal, and the ion flux distribution across the channel is no longer uniform when the ions exit (Figure 3-3(b)).

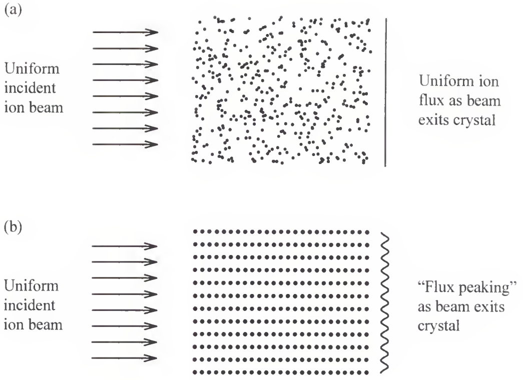
(a)
Uniform incident ion beam
Uniform ion flux as beam exits crystal
(b)
Uniform incident ion beam
"Flux peaking" as beam exits crystal

Figure 3-3. Influence of beam incidence on ion flux as beam exits crystal. a) random incidence (or amorphous material); b) aligned incidence.

The detailed shape of this flux distribution varies with small changes in the incident angle of the beam. When the beam enters with no tilt relative to an axial channeling direction, the flux distribution is strongly peaked in the center of the channel upon exiting the crystal. As the crystal is tilted outward by tenths or hundredths of a degree at a time, the flux distribution gradually flattens out until at a tilt of ~1° (for 2.5 MeV He^+ in Si), the flux is uniformly distributed across the channel, as it is for random incidence. This narrow range of tilt angles points out the existence of a critical angle for channeling and demonstrates the requirement for small beam divergence in channeling, as mentioned in Chapter 2. At tilts greater than the critical angle, the ions penetrate too closely to the host atoms to be steered by the correlated, small-angle collisions.

As an individual ion traverses the crystal, it undergoes a series of small-angle collisions with the atoms that compose the rows or planes of the channel "wall." The channeled ion interacts with the screened Coulomb potential of the nuclei and thus does not penetrate closely enough to experience large-angle Rutherford scattering or a nuclear reaction. Successive collisions are correlated, as the scattering angle from one collision determines the incident angle for the next, and the ion undergoes transverse oscillations in the channel. Because of the small scattering angle of each collision, these oscillations occur with a period corresponding to collisions with hundreds of atoms. (The large scale of these oscillations allows for the rows and planes of individual atoms to be approximated as continuous strings and planes. This continuum model, formulated by Lindhard [Lind65], will be discussed further in Chapter 4.) Although not to scale, Figure 3-4 illustrates the channeling process and shows that the amplitude of transverse oscillations varies with an ion's initial position as it enters the channel.

The energy loss of ions, due largely to interactions with the electrons in the target material, also varies with initial position in the channel as well as with tilt angle. For axial alignment, the ions incident near the middle of the channel spend most of their time near the middle (Figure 3-4), where the electron density is low. Those that enter near the atom rows pass closer to the host nuclei, experience higher electron densities and hence lose more energy than the ions that travel through the middle. These different rates of energy loss indicate that, in addition to the flux, the ion energy distribution is non-uniform as a channeled beam exits a thin crystal. The higher energy ions will be concentrated near the

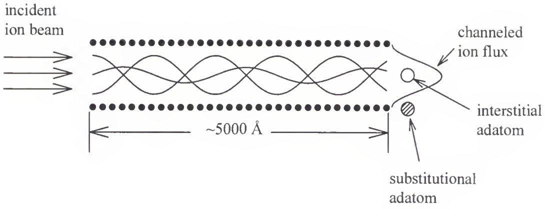

Figure 3-4. Model of channeled ion beam showing overlap of adatom positions with ion flux as beam exits crystal. (The model is not to scale.)

middle of the channel (an important point that will be considered further in the next section and in Chapter 4). As the sample is tilted from the axial direction, the difference in energy loss across the channel gradually diminishes until it, like the flux distribution, becomes uniform for random alignment.

Straggling is another process that broadens the ion energy distribution as the beam transits the sample. Even when the beam is incident on the sample in the random direction, the ions emerge from the exit side of a thin sample with a spread in energy because of statistical fluctuations. As an ion travels through the sample, it loses energy incrementally through many separate encounters. Each ion in the initially monoenergetic beam will experience a unique set of encounters and thus will have a slightly different energy loss than other ions. Energy straggling results in decreased mass resolution because of overlapping peaks in the energy spectrum (see next section) of ions scattered from atoms whose masses differ by a small amount.

Ion Scattering

To obtain useful data for analysis of surface structure, transmission ion channeling depends on the elastic, binary collisions of the channeled ions with the adatoms on the beam-exit side of the crystal. The basic phenomenon for 2.5 MeV He^+ ions scattering from Si, Ge, and Sb is classical, Rutherford scattering, in which an incident ion scatters at a large angle because of the repulsive force between the ion and a target atom nucleus. The energy of scattered ions can be derived easily from the equations for conservation of energy and momentum. In practice, the kinematic factor, which is the ratio of the scattered ion energy to the incident ion energy, is used. The kinematic factor, K, depends only on the scattering angle and the masses of the ion and the target atom. For a given ion, K increases with the mass of the target atom, allowing for identification of species in the sample by their position in the energy spectrum of scattered ions. (See Figure 4-1 in the next chapter for sample spectra showing this separation in scattered ion energy for different target atom masses.)

As mentioned above, the ions undergo Rutherford scattering; that is, the probability of scattering is given by the classical, Rutherford scattering cross section, $d\sigma/d\Omega$. This differential scattering cross section is directly proportional to the squares of the atomic numbers of ion and target atoms and inversely proportional to the square of the ion energy and, approximately, the fourth power of $\sin(\theta/2)$. For a detector that subtends a small solid angle, Ω, the net cross section is well-approximated by the average cross section multiplied by the solid angle, $\langle d\sigma/d\Omega \rangle \Omega$. Rutherford scattering cross sections are easily found for the scattering events in our experiments, and are necessary for determining adsorbate coverage and for simulating energy distributions of scattered ions (Chapter 4).

These two concepts, the kinematic factor and the scattering cross section, form the basis for the analysis of ion scattering data. The kinematic factor, as mentioned above, describes the separation in the energy spectrum of ions scattered from different masses. The importance of the cross section in transmission ion channeling stems from the dependence of the yield of scattered ions on the overlap of the cross section with the ion flux distribution. For ions scattered from the beam-entrance surface, the ion flux distribution is uniform and hence the yield has no dependence on the sites of the adatoms. For ions scattered from the beam-exit surface, however, the ion flux distribution is not uniform, with the result that the scattering yield is site-dependent.

Figure 3-4 shows two possible adatom sites (on a one-dimensional surface), one at the end of an atom row (substitutional) and one in the middle of the channel (interstitial). (The inset of Figure 3-5 shows these two sites and a dimer site in a top view of the two dimensional Si(100) surface.) Clearly, the substitutional site will produce a low yield of scattered ions, whereas the interstitial site will produce a high yield. As the beam-sample alignment is gradually tilted away from the channeling direction, the ion flux distribution flattens out and the yield shows less dependence on adatom site. Finally, at random incidence, the yield of scattered ions shows no site dependence at all, as the yield from all adatoms of the same type is the same. Plots of the yield versus tilt angle (an angular scan) for the substitutional and interstitial sites, as well as an intermediate (dimer) site, are shown in Figure 3-5. The yields shown have been normalized to the random yield for easy comparison. An adsorbate randomly distributed on the surface would produce a flat angular scan with a normalized yield of 1.0 all the way across.

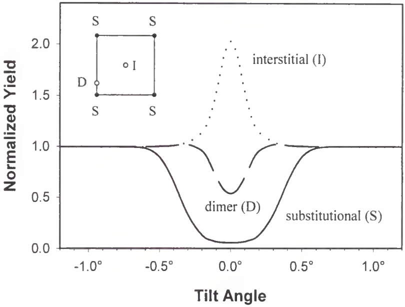

Figure 3-5. Angular scans for three different types of adatom sites. The inset shows the three sites in the Si(100) surface plane.

In addition to the site-dependence of the ion scattering yield in transmission channeling experiments, the scattered ion energy distributions vary with adatom position on the surface. As discussed in the previous section of this chapter, the two types of ion trajectories shown in Figure 3-4 illustrate the different rates of energy loss as ions traverse the sample. Ions that stay near the middle of the channel emerge with higher energy than those that penetrate closer to the atom rows. The result of this energy loss discrepancy is that all of the higher energy ions can be found near the middle of the channel in the peak of the ion flux distribution. Thus, not only will an interstitial adatom produce a higher ion scattering yield than adatoms nearer the host atom rows, but it will also cause a shift to higher energy in the scattered-ion energy distribution. Both of these outcomes can be seen in Figure 3-6, which shows the scattered ion energy distributions for interstitial, dimer, and substitutional sites.

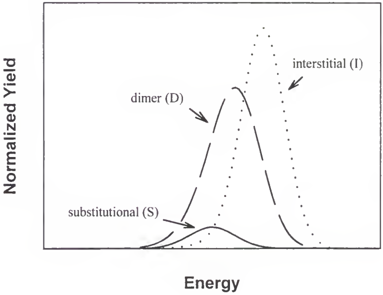

Figure 3-6. Scattered ion energy distributions for three different types of adatom sites.

CHAPTER 4
DATA COLLECTION AND ANALYSIS

Data Collection

Each experiment begins with the procedure for finding the middle of the thin window in the sample by translating the sample vertically and horizontally in a plane normal to the ion beam. The beam will pass through the sample and illuminate the piece of quartz at the end of the beamline until the thick part of the sample intercepts the beam, after which the beam is no longer visible on the quartz. Once we have found the middle, we have a reference point for finding the five spots that we use on the thin window. With the sample oriented so that the adsorbate-covered surface faces the beam, we take a set of five backscattering spectra for the purposes of monitoring the adsorbate coverage and checking for the presence of contaminants.

Upon completing the backscattering spectra, we rotate the sample 180° so that the adsorbate-covered surface is on the beam exit side of sample. We then align the beam with the channeling direction (<100> or <110> for the work described herein). To achieve this alignment, we generally start near the same A (rotation angle about the vertical axis) and C (rotation angle about the horizontal axis) values where we last found the channeling direction and then monitor the pattern on the piece of quartz at the end of the beamline while changing A and C. As the beam incidence angle nears a major plane in the crystal, a blocking pattern appears on the quartz because of shadowing [Fel82].

When the beam is aligned with the plane, a bright spot appears due to channeled ions hitting the quartz. By following the {100} and {110} planes to their intersection, we find the <100> channeling direction.

Comparison of Si yields with simulations has shown that the accuracy of alignment is 0.02°–0.05° for this visual method of beam-sample alignment. Also, since the Si(100) sample cleaves along {110} planes, the relative orientation of the blocking pattern and the sample edges provides a check that the plane we indicate as the {110} plane by the size of its blocking pattern is indeed that plane. Another point to note here is that the time it takes to find the channeling direction is only about five minutes, short enough that the sample suffers little degradation during the procedure.

The next step is to tilt the sample by ~8° in A away from the <100> channeling direction and find the {100} plane. The A and C values for this point and for the <100> channeling direction serve as reference points so that for any crystal coordinates, θ and ϕ, we can find the corresponding laboratory coordinates, A and C, by using the methodology of Dygo *et al.* [Dyg93]. The angle θ is the tilt away from the channeling direction, and the angle ϕ is the azimuthal angle around the channeling direction. Thus, some commonly used values of (θ, ϕ) are (0°,0°) for the <100> channeling direction, (6°,0°) for the {100} plane at a tilt of 6°, (6°,45°) for the {110} plane at a tilt of 6°, and (6°,30°) for random incidence near the <100> channeling direction.

This procedure is used to find the directions for both angular scans and individual energy distributions at select points. In the case of angular scans, such a precise knowledge of the points in the scan obviates the need for azimuthal averaging at each tilt angle, a time-consuming procedure often undertaken to eliminate planar channeling influences. We simply choose to tilt the sample in a direction with minimal planar effects, as shown by simulation of the ratio of the mean energy loss to the random energy loss for various values of θ and ϕ [Bos96a]. Good directions so indicated include 15° from the {110} plane for a <100> scan and 10° from the {100} plane for a <110> scan. In collecting data for analyzing individual energy distributions, we have used three directions almost exclusively: the <100> channeling direction, the {100} plane at a tilt of 6°, and random incidence. We also collected data for beam incidence along the {110} plane at a tilt of 6°, but, for reasons given later in this chapter, we have had to discard those data. More details about the beam-sample alignment procedure are given in Boshart's Ph.D. dissertation [Bos96a].

Each spectrum is taken for a specific dose of integrated beam charge, as collected by the Faraday cup at the end of the beamline. The current integrator feeds a pulse into the multichannel analyzer for each 10^{-5} μC of integrated beam current, correcting for the average charge state (+1.94) of He ions upon emerging from the Si. Both the dose and the beam current must be monitored to minimize damage to the Si crystal. We generally bombard the sample with a current of ~10 nA and keep the total dose on one analysis spot on the sample to ~200 μC. (This total dose corresponds to a fluence of $\sim 10^{17}$ ions cm^{-2}.)

A problem that sometimes occurs for certain positions of the goniometer and sample module is blocking of one or more of the detectors. For example, with the sample in transmission geometry, the clips that hold the sample on the module can prevent some or all of the scattered ions from reaching the 79° detector, and the sockets that hold the module legs can block the 150° detector. When the sample is in backscattering geometry, the 70° detector is always blocked by the back of the goniometer, but in this case it does not matter because we are interested only in backscattering, that is, spectra recorded by the 150° detector.

As discussed in Chapters 2 and 3, the data collected are either scattered helium ions or recoiled hydrogen atoms. Figure 4-1 shows two spectra of scattered helium ions for a Ge/Sb/Si(100) sample. The vertical axis in the graph shows the number of scattered ions and the horizontal axis represents the energy of the ions. (Calibration of the energy axis will be discussed in the next section.) These spectra show the raw data collected for <100> and random beam incidences.

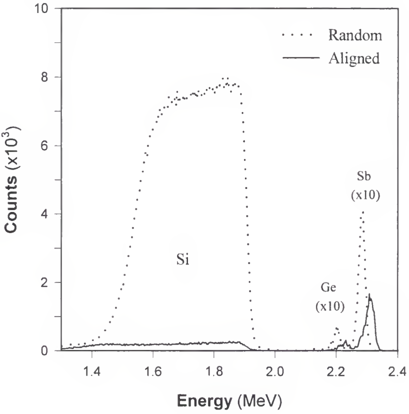

Figure 4-1. Sample spectra from the 79° detector showing the Si, Ge, and Sb peaks for random and aligned (<100> in this case) beam incidences.

Data Analysis

The work presented in this dissertation falls into two categories: the H/Ge/Si(100) study (Chapter 6) with analysis of angular scans based on the continuum approximation and the surfactant-mediated growth study (Chapter 5) that relies on fitting energy distributions with a Monte Carlo channeling simulation. The two analysis methods will be discussed separately in this section, preceded by an explanation of the data analysis steps that are common to both methods.

Preliminary Analysis

The first step in analyzing the data is to calibrate the energy axis (i.e., convert channel numbers to energies on the horizontal axis) in the spectra taken with the 150° detector. This calibration can be done in one of two ways, depending on the nature of the sample being studied. The most common method makes use of the spectra taken with the sample in backscattering geometry. In this case, the helium ions that backscatter from surface atoms have an accurately known incident energy, E_0, and lose no energy in the sample. Hence, these ions enter the detector with energy $E_1 = K\ E_0$. The kinematic factor, K, (discussed in Chapter 3) depends on the masses of the ion and target atom and on the scattering angle and is easily calculated. Thus, the channel numbers of two known peaks in the spectrum are sufficient to calibrate the axis, as the relation between channel number and energy is linear [Chu78]. Typical values are 2-3 keV per channel for the slope of this linear relation and ~100 keV for the intercept.

The disadvantage of using the backscattering geometry spectra to calibrate the energy axis is that we generally obtain these spectra at a low dose (~5 μC). For adsorbate coverages in the monolayer range, the low dose means poor counting statistics and greater uncertainty in the channel number. For the experiments done with Sb on the sample, however, we can use the transmission geometry spectra because a small amount of Sb adsorbs on the etched side of the sample. This Sb produces a peak in the backscattering spectra that can be used, along with the Si peak, for the calibration. Figure 4-2 shows such a spectrum.

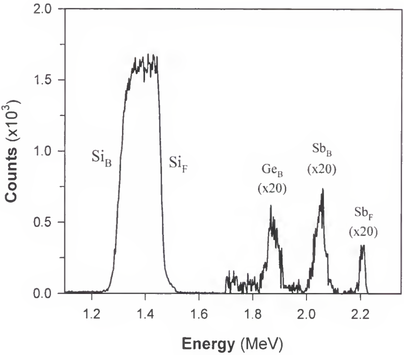

Figure 4-2. A spectrum from the 150° detector with the sample in transmission geometry and Sb on both sides of the sample. The subscripts "F" and "B" refer to the surfaces at beam incidence (front) and exit (back).

The second step is to find the thickness of the Si thin window. With the sample oriented for random beam incidence, the width of the Si peak in the spectrum from the 150° detector is proportional to the Si thickness. After obtaining the energy calibration as described above, we can find the energy corresponding to the half-height of the low energy side of the Si peak (labeled Si_B in Figure 4-2). This energy represents the detected energy of ions that scatter from the back side of the sample. The initial energy of these ions has been decreased by three processes: (i) traversing the Si from front to back, (ii) undergoing Rutherford scattering from a Si atom on the back side of the sample, and (iii) traversing the Si from back to front. By using the results of experimental energy loss measurements of helium ions in Si [Zie77] and the kinematic factor, we can find the thickness of Si that will yield this detected energy [Bos96a]. (In the section on the Monte Carlo channeling simulation method of analysis, another way to determine the thickness will be presented.)

The third step is to calculate the adsorbate coverage on the surface. This is a straightforward calculation because the yield, Y, of backscattered ions depends on the scattering cross section, σ, the solid angle of the detector, Ω, the number of incident ions, Q, and the adsorbate areal density, N_s, as follows: $Y = \sigma \Omega Q N_s$ [Fel86]. Because the Rutherford scattering cross sections are known so accurately, this formula can provide areal densities to within ±10%. The solid angle is known from measurements of the aperture covering the detector and the distance between goniometer and detector. The number of incident ions comes from the current integration, and the yield of backscattered particles is the sum of counts in the peak of interest. The areal density is related to coverage in monolayers on the Si(100) surface by the conversion factor 1 ML = 6.78×10^{14} atoms cm^{-2}. (This is the number of Si atoms in the top layer of the Si(100) surface.)

The final step that is common to both analysis methods is to determine the scattering yield from the adsorbate(s) for each spectrum that will be included in the angular scan or the Monte Carlo fitting procedure. To find the net number of counts, we sum the counts in a peak and subtract the appropriate number of background counts, which are found by summing the counts on each side of the peak in a number of channels equal to half the number in the peak. In some cases, the background must be subtracted more from one side of the peak than the other because of proximity to other peaks (e.g., Si), but in all cases, the total number of background channels equals the number of peak channels.

Other methods of accomplishing background subtraction include (i) fitting the background to a line and subtracting the area under the line from the summed counts in the peak and (ii) fitting the background to a line and the peak to a set of gaussians and finding the net area of the peak. Both yield similar results to the aforementioned method. Chapter 5 presents our work on Ge and Sb on Si(100), and, as can be seen in Figure 4-1, the Ge and Sb peaks overlap slightly. For the separate analysis of the two adsorbates, this overlap creates a problem and the best solution is to use a peak-fitting procedure [Gra94a]. In our case, however, we are not trying to extract an accurate yield from each peak to plot Ge and Sb separately in an angular scan. We are fitting the two peaks simultaneously, so the total yield of the two peaks is sufficient [Bos96a].

In the end, the net number of counts for each spectrum is divided by the number of counts from the random spectrum. This number is called the normalized yield and is used for both angular scans (with a slight correction discussed below) and energy distributions. We check the validity of our results by comparing the normalized yields obtained from all three detectors and also by checking the normalized yields for the Si. (The normalized Si yields for the most common directions should be ~4% for <100>,

~40% for {100}, and about 25% for {110}.) By monitoring the Si yield, we sometimes spot slight blocking in a detector that we may not have noticed otherwise.

Angular Scans and the Continuum Approximation

As mentioned in Chapter 3, transmission ion channeling data for adsorbate site determination comes in two flavors: energy distributions of scattered ions and plots of ion scattering yield versus tilt angle near a channeling direction. In this section, we discuss the latter. The basic idea of this method is to compare experimental angular scans to calculated scans. It is easy to see from Figure 3-5 that we can make qualitative statements about the surface structure by inspection of the experimental data, but an accurate site determination depends on quantitative analysis. Mark Grant, who first put this quantitative analysis to use in our research group, has described the method in greater detail than will be done here [Gra94a].

A beam of channeled ions emerges from the back side of a thin crystalline sample with a nonuniform flux distribution. The shape of this distribution, which changes with tilt angle, can be calculated and used for quantitative analysis of angular scans. We use a computer program written by Bech Nielsen [Bec88a, Bec88b] for these calculations. To generate these distributions, the program uses the continuum approximation, which treats the rows of atoms in the crystal as continuous lines and was first proposed by Lindhard [Lind65]. The program also assumes statistical equilibrium, that is, uniform probability density of channeled ions within their energetically accessible regions. This assumption is also due to Lindhard [Lind65]. Two other important features of this program are the use of the Doyle-Turner 25-string potential [Doy68] and the incorporation of a model for dechanneling. The latter feature is accomplished through the use of a diffusion-like equation that considers both electronic and nuclear dechanneling and is responsible for this program giving better results than earlier calculations that used the continuum approximation [Bec88a, Bec88b].

Some drawbacks in using this method center around the assumption of statistical equilibrium. First, statistical equilibrium is not always reached. Upon entering the crystal, the ions oscillate within the channel and cause the scattering yield from substrate atoms to vary as a function of depth [Fel82]. Thus, for an extremely thin crystal, the adsorbate scattering yield would be a function of depth. The solution to this problem is to use a crystal that is thicker than ~2000 Å. Another problem is that continuum model calculations will underestimate the scattering yield in the channeling direction [Barr71, Barr76]. For the worst case (i.e., when the adatoms are in substitutional sites), the error in the normalized yield is only ~2% and is accepted as a limitation of the method [Gra94a, Sei93].

To calculate the scattering yield from an adsorbate, the program overlaps the ion flux distribution with a gaussian distribution that represents the adatom site and accounts for dechanneling. The relevant parameters required as input for the program are the beam energy, dose, tilt angle, sample thickness, adatom vibrational amplitude, and adatom position. The first three of these are determined during the experiment, and the thickness is calculated as explained in the previous section. The vibrational amplitude and the adatom position are variables to be determined in the analysis. In practice, because the vibrational amplitude is difficult to ascertain, we usually assume isotropic and enhanced values for this quantity and use values from the literature when they are available.

Although atoms on the surface generally have an enhanced vibrational amplitude [Woo94], few studies have looked at the vibrational properties of adsorbates.

To find the adatom position, the program iterates over all reasonable values until we find the best fit as determined by the minimum χ^2 goodness-of-fit value. The adatom positions used as input for the program are given as fractions of a lattice constant, *a* (5.431 Å), and referenced to the positions in the <100> channel. The program can accommodate two different sites as input to account for adsorbate structures such as asymmetric dimers. Also, because of the two types of terraces on the Si(100) surface with dimers rotated 90° relative to each other, the program must consider sites on both kinds of terraces. For the <100> direction, each site on the surface must be treated as two equivalent sites. In the <110> direction, each site gives rise to four equivalent sites.

Before we can compare the experimental and calculated angular scans, however, we need to make a small correction to our experimental scattering yields, as alluded to in the previous section. The problem is that the energy loss difference between channeled and random (non-channeled) ions affects the scattering cross section. Channeled ions will have higher energy than random ions and thus a lower cross section. (For Rutherford scattering, $\sigma \propto 1/E^2$.) The result is a decrease in the scattering yield in the channeling direction. Lyman has found that the reduced yield can cause an amorphous Ge layer to exhibit a channeling dip, even though the normalized yield is expected to be flat all the way across the scan [Lym91a]. The correction involves scaling the yield to account for the difference in cross section and weighting the correction to account for the relative amounts of channeled and random ions. These corrections typically increase the normalized yield by ~3% in the <100> channel and ~6% in the <110> channel [Gra94a].

Energy Distributions and the Monte Carlo Simulation of Channeling

In analyzing ion scattering data by fitting angular scans as described in the previous section, we extract only the net yield from a particular peak in each spectrum. In this section, we will look at how we now utilize the information carried in the shape and position of the energy distribution of scattered ions (Figure 4-3). The key to this new method of analysis lay in changing from the analytical calculations based on the continuum approximation to a Monte Carlo simulation of the channeling process. Andrzej Dygo developed the Monte Carlo program, and Mark Boshart helped him to implement an energy loss model so that the output of the program is a distribution of not only ion positions but also ion energies. The ion distribution is then overlapped with trial adatom sites to generate simulated energy distributions of scattered ions. These, then, are the two main components of our analysis procedure: (i) generating ion distributions with the Monte Carlo program, and (ii) using these ion distributions to simulate energy distributions with the "site" program.

The Monte Carlo program that Dygo brought to the University of Florida when he worked in our research group in 1993-94 was the CXX code [Dyg88, Dyg89, Dyg94b, Dyg94c]. This program follows ion trajectories through a crystal by calculating the effects due to screened Coulomb interactions, multiple scattering by electrons, energy loss processes, surface layers, incident beam angular divergence, and host atom thermal vibrations. Dygo and Boshart then added improvements to the energy loss component of the code by fitting experimental energy distributions for H^+ and He^+ scattered from an amorphous Au layer on Si [Dyg94a, Bos95b, Bos96a]. They found that by employing the semiclassical approximation model for core electrons and the free electron gas model for

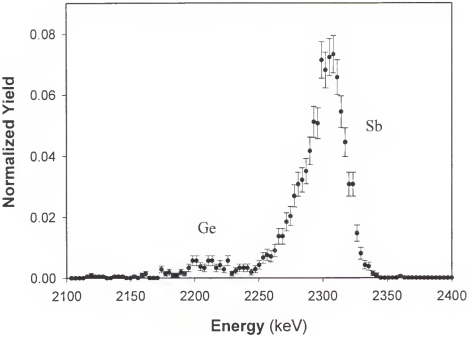

Figure 4-3. Scattered ion energy distribution with error bars.

valence electrons (adjusting each model by several percent), they obtained good fits to the experimental data.

The "Monte Carlo" aspect of the program is the random placement of an ion in the channel to begin the simulation. This initial position then determines the starting impact parameter, and it is this quantity that is used in calculating the trajectory and energy loss as the ion penetrates into the crystal. To calculate the ion-host atom interactions, the program uses a Hartree-Fock potential modified for solid state electronic densities [Dyg92, Smu92], and the calculation proceeds one layer at a time. Since all of the analysis discussed in this dissertation is based on the use of a 2.5 MeV He^+ beam incident on Si crystals, the only inputs required are the number of ions to simulate (usually 20,000), the beam incidence angle and the Si thickness. The output, then, is a distribution of ion positions and energies. Figure 4-4 shows typical distributions of ion positions for He^+ ions incident in the <100>, {100}, and random directions. (The {100} and random incidences are at a tilt of 6° to the <100> direction, and the circles at the corners represent the Si atom rows.) Each of the ions in these distributions also has an energy, the knowledge of which makes simulating energy distributions possible.

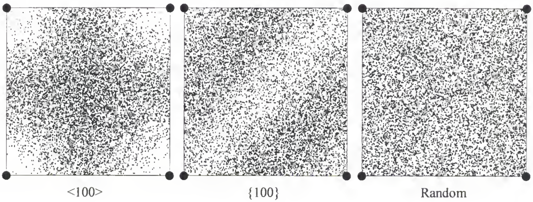

Figure 4-4. Distributions of helium ion positions after the ions have traversed 6000 Å of Si with the directions of beam incidence indicated.

Before we are ready to make use of the Monte Carlo simulated ion distributions for surface structure determination, however, there are a few more steps in the preliminary analysis. As detailed earlier in this chapter, we have already calibrated the energy axis for the 150° detector, used this calibration to find the Si thickness, calculated the adsorbate coverage, and extracted the net yield from the adsorbate peaks. The next step is to calibrate the energy axis for the 79° detector. (We use the spectra from this detector rather than from our other transmission detector at 70° because of the greater separation, due to kinematics, between the Si, Ge, and Sb peaks.)

This calibration is not as straightforward as for the 150° detector because the scattered ions have lost energy by traversing the Si crystal as well as in the close encounters with nuclei that sent them to the detector. For a random spectrum as is shown in Figure 4-1, we can use the Si, Ge, and Sb peaks for calibration, but we first must know the energy of the ions just before they scattered and which side of the Si peak to use. To address the latter issue, we only need look at the geometry. For ions that scatter from Si atoms at the beam entrance surface, the path length, d_F, through the Si is longer than the path length, d_B, of those that scatter from Si atoms at the beam exit surface (Figure 4-5). The front-scattered ions therefore lose more energy and contribute to the low energy Si edge in the scattering spectrum. The ions that scatter from Si on the back surface, where the Ge and Sb also reside, make up the high energy edge of the Si peak. The former issue (ion energy before scattering) can be answered in the same manner that we found the Si thickness previously: We use the aforementioned empirical energy loss data [Zie77], along with the Si thickness, to find the ion energy. With this post-transit, pre-scattering ion energy, we then use the channel numbers of our known peaks and the kinematic factors to obtain the energy calibration parameters.

The next stage of analysis is to prepare the experimental data files for use by the site program. We choose a suitable range of channels, apply the energy calibration, and normalize the yield. The yield at this stage, however, is not normalized to the random yield. The number of counts in each channel of a particular energy distribution is divided by the total number of counts for *that* energy distribution. The distribution also is scaled by a factor that accounts for the difference between the width of the channels in the experimental energy distribution and the bin width of the simulated energy distribution.

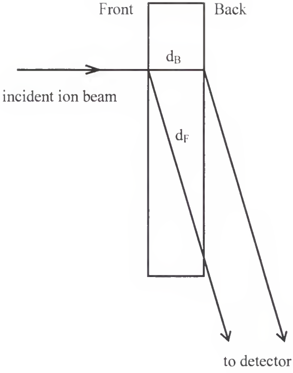

Figure 4-5. Scattering geometry showing the longer path length for ions scattered from the front of the sample than for those scattered from the back of the sample.

For computing purposes, the normalized yield is incorporated into the simulated energy distribution by the site program. One more task necessary at this stage is fitting the experimental background. Over the range of energy in the experimental energy distribution, the background is approximately linear and a numerical fitting procedure [Bos96a] determines the slope and intercept. These parameters are later used to add the appropriate background level to the simulated energy distributions.

With experimental data in useable form, we can start the fitting procedure. The first step here is to obtain a good fit to the random data (i.e., the spectrum obtained when the beam is incident in the random direction). These data contain no structural information because of the uniform ion flux distribution. What we find is that the thickness obtained in the manner explained earlier is inadequate. In almost every case, our first attempt to "fit the random" results in a simulated energy distribution that is shifted to the left or right of the experimental energy distribution. By trying different thicknesses, we eventually obtain a simulated energy distribution that overlaps the experimental one (Figure 4-6).

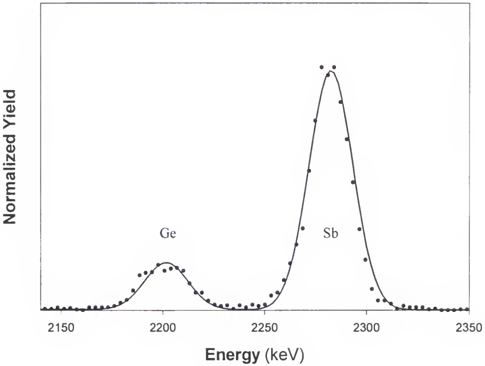

Figure 4-6. An experimental energy distribution (dots) for the random direction and a good fit (solid curve) from the site program.

Normally the thickness obtained in this manner differs from the previous thickness by less than 100 Å. If the new thickness differs by more than 100 Å from the earlier one, we generally do not use those data because of problems with energy calibration. (Recall that the 79° detector was calibrated based on the previously found thickness. Therefore, using a significantly different thickness would indicate the need for a new calibration, which would have an effect on the thickness. In the end, we would have to iterate over a number of thicknesses, correcting the energy calibration each time, to find the correct value. Because this problem affects only a small portion of our data, however, we simply discard those with thickness discrepancies larger than 100 Å.)

In addition to obtaining a more accurate Si thickness by fitting the random, we also establish the values for two other parameters. First, we determine the full width at half maximum (FWHM), a measure of the energy resolution, that best fits the peaks. The FWHM is typically 25 to 30 keV. Finally, for the case of fitting two peaks at once, we often slightly adjust the ratio of the coverages to obtain a better fit.

To continue the discussion of fitting experimental data with simulated energy distributions, we need to examine in more detail how the site program operates. Basically, the program reads in the ion positions and energies, simulates a scattered ion peak based on the distance between the ions and the trial site, and then compares this simulation to the experimental data. Reading in the ion distribution is a straightforward process: the ion positions are transformed to account for different coordinate systems in the Monte Carlo and site programs and then the x, y, and E values are put into separate, one dimensional arrays.

Simulating an energy distribution occurs in several phases. The equivalent sites (due to the two types of terraces on Si(100)) for a trial adatom site must be considered, as must equivalent sites for proper overlap with the ion distribution. Then for each site considered, the program finds the distance in the x-y plane between the site and each ion in the distribution. Treating the trial site as a gaussian distribution, the program uses this distance to add a contribution, $wCe^{-(d/\rho)^2}$, to the scattered ion peak. Since the site program can consider up to eight different sites, the contributions for each are scaled by the weight, w, given to that particular site. The factor, C, is a correction for the differing cross sections at different ion energies and is equal to $(E_0/E_{ion})^2$, and ρ is the two-dimensional vibrational amplitude. One more important point in the operation of the program is that only the ions that lie within a distance of twice the vibrational amplitude are calculated in the yield in order to speed the computations.

So far we have accounted for the ion contributions to the yield, but to create an energy distribution, we must also keep track of the energy of each ion that undergoes (simulated) scattering. To do so, the program multiplies the energy of the ion by the appropriate kinematic factor (for Ge or Sb) and puts the yield and energy information into an array. In addition to looping over all of the ions and the equivalent sites, the program also has the capability to iterate over a particular value of x, y, z, or ρ.

After all of the looping and iterating is done, we have an array of yield and energy values, but this array is not yet ready for comparison with the experimental data. The next steps are to add in the effect of energy straggling, smooth the data, add the linear background to match that of the experimental data, incorporate the energy resolution (FWHM), and then normalize the yield. The yield is normalized first by dividing the number in each energy bin by the total from the simulated random energy distribution and then by dividing by the experimental normalized yield. (The latter division is because each experimental energy distribution was normalized to itself rather than to the random yield, as explained earlier.)

At this point, the simulated yield and energy values are compared to the experimental energy distribution and also written to an output file. To make the comparison quantitative, the program calculates the goodness of fit using the following equation:

$$\chi^2 = \sum_i \frac{(N_i - n_i)^2}{n_i} \qquad (4\text{-}1).$$

In this equation, N_i is the simulated yield and n_i, the experimental yield. The χ^2 values thus calculated allow for comparisons of various simulated distributions for one spectrum but do not yield absolute values that can be compared with fits to other spectra.

This method of comparing simulated to experimental energy distributions has distinct advantages over the analysis of angular scans described in the previous section. First, we utilize all of the scattering information available in a spectrum. Instead of simply making the sum of a peak one point in an angular scan, we use the shape and position of the energy distribution as well. As an added benefit, this extra information allows us to forego angular scans altogether and take fewer spectra at higher doses.

Naturally, this method also has disadvantages. Two of these drawbacks, which will be discussed in greater detail in the next two sections, are planar oscillations for beams incident in the {110} direction and variation of the Si thickness. The former is evidenced by an ion flux distribution that changes dramatically as a function of depth. The latter is a problem that can create difficulty in the interpretation of the fits in some cases.

{110} planar oscillations

An interesting feature of simulated energy distributions emerged during an attempt to make a correction for thickness variation (discussed in the next section). Simulations for two different sites being compared to the same set of {110} planar data underwent a dramatic and unexpected shift relative to the experimental data and to each other (Figure 4-7). In going from a Monte Carlo ion distribution for a thickness of 5125 Å to a distribution for a thickness of 5400 Å, one of the simulations (site A) increased in yield whereas the other (site B) displayed a decreased yield. A closer look at other data and simulations showed similar occurrences for this direction of beam incidence.

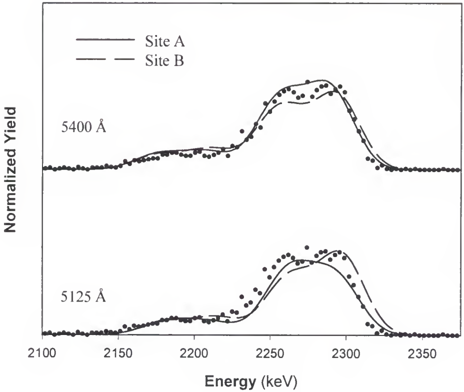

Figure 4-7. Simulated energy distribution flip-flop. The same set of experimental data (dots) plotted against simulations for two different sites (solid & dashed curves) at two slightly different thicknesses (upper & lower simulations).

Because the only difference between the two simulations was the use of two different thicknesses, a look at the ion distributions should show the cause of the yield flip-flop. Figure 4-8 shows the ion distributions responsible for the above simulated energy distributions, and indeed the problem is evident. The important feature to notice about these ion distributions is that the band of planar channeled ions in the center is broader and less dense for the 5400 Å distribution shown in Figure 4-8(a) than for the 5125 Å distribution in Figure 4-8(b).

By examining which ions are responsible for the two simulated energy distributions, we can understand the yield flip-flop. The large black circles in Figure 4-8 enclose the ions that are sampled for the site A energy distribution, and the large white circle in the near-interstitial site encloses the ions that contribute to the site B energy distribution. (The size of these circles is two times the 2D vibrational amplitude, as only the ions within that range are considered.) The narrow band in the 5125 Å distribution puts a higher density of ions in the white circle and a lower density in the black circles than does the broader band in the 5400 Å distribution. That variation in the number of ions within each circle results in the reversal in the relative yields for the two sites.

As can be seen from the examples shown in Figure 4-9, the changing ion distribution is not unique to the two thicknesses discussed in the previous paragraphs. For the three distributions shown in this figure, the band of channeled ions starts out broad in part (a), reaches a minimum width in part (b), and then is expanded again in part (c). The ion distributions for {110} incidence actually exhibit this oscillatory behavior over the whole range of sample thickness (3000 Å to 6000 Å) in which we are interested. The relatively short wavelength of these oscillations (~700 Å) creates difficulty in our data

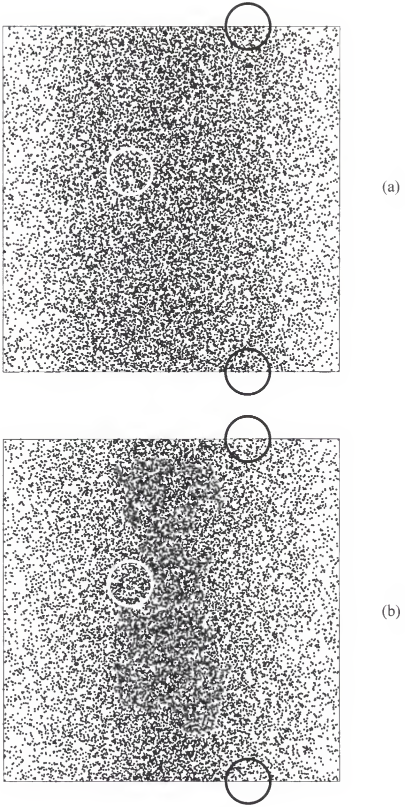

Figure 4-8. {110} ion distributions for (a) 5400 Å and (b) 5125 Å.

analysis because our problems with thickness variation are compounded by the changing shape of the energy distribution. In order to use the {110} data, we would have to know the thickness to within ±50 Å, a resolution that is difficult to attain.

This phenomenon has been documented by Abel *et al.* in a study of oscillations of backscattering yield in planar directions[Abe75] and also by Breese *et al.*, who have imaged these oscillations directly in a transmission channeling experiment using a nuclear microprobe with 3 MeV protons [Bre96]. Oscillation of individual ions in a channel is discussed in the section on ion channeling in Chapter 3 and is responsible for the oscillation of the band of {110} planar channeled ions discussed here. This effect implies that the individual, oscillating ion trajectories remain coherent with each other. Furthermore the variation in oscillation wavelength among the different ions is small enough not to damp out the oscillations.

The observation of these oscillations for beams incident in the {110} direction raised the question of whether the other directions of beam incidence that we use would show the same effect. An appeal to the dimensions involved should at least partially allay our concerns for the other planar direction that we study. The {110} channel has a width of 1.92 Å, whereas the {100} channel is 1.36 Å across. This smaller channel will cause the oscillations to damp out much more rapidly. For <100> axial channeling, the ions lose coherency even more quickly because of being constrained in two dimensions rather than one. Indeed our hunch that the <100> and {100} directions do not show this oscillatory behavior is borne out by inspecting the Monte Carlo ion distributions, shown in Figure 4-10 and Figure 4-11 respectively.

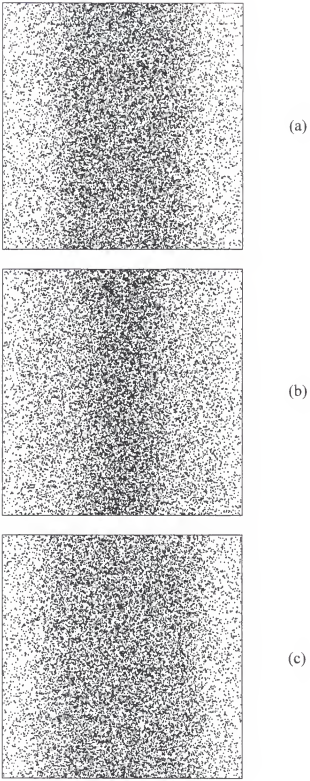

Figure 4-9. {110} ion distributions for Si thicknesses (a) 3300 Å, (b) 3600 Å, and (c) 3900 Å.

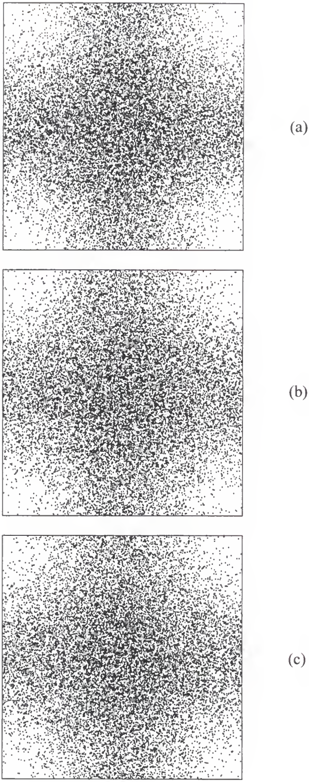

Figure 4-10. <100> ion distributions for Si thicknesses (a) 3300 Å, (b) 3600 Å, and (c) 3900 Å.

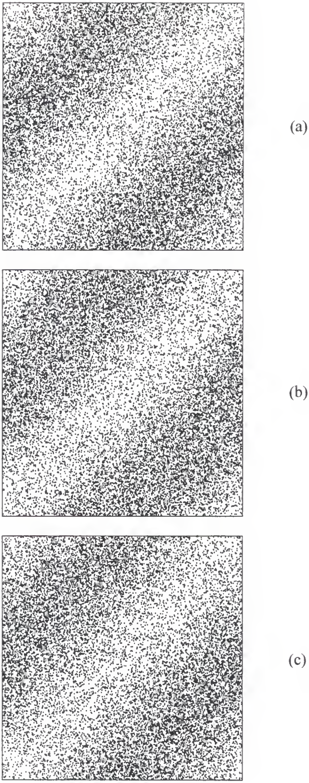

Figure 4-11. {100} ion distributions for Si thicknesses (a) 3300 Å, (b) 3600 Å, and (c) 3900 Å.

Thickness variation

For the method of fitting simulated to experimental energy distributions to give meaningful results, accurate knowledge of the Si thickness is essential. Without such knowledge, we obtain simulated energy distributions that often are shifted on the energy axis relative to their experimental counterparts. The reason for this effect is that the Ge and Sb peak positions on the energy axis, as well as the energy calibration of the 79° detector, depend on the Si thickness. The yield (and the shape) of the two distributions may differ little, but the energy shift can make interpretation of the results difficult or impossible. (For the case of {110} beam incidence, however, the shape also can differ greatly because of the planar oscillations described in the previous section.) In this section we will look at how Si thickness variation shows up in our data and how we can correct for it.

Before we investigate the manifestation of Si thickness variation, we need to examine its origin. To do so, we must recall the details of producing the thin windows. As stated in Chapter 2, we use a chemical etch procedure in which the etchant stops when it reaches a boron layer that has been diffused into the Si from the opposite side of the sample [Che80].

Two factors in this process are largely responsible for all observed thickness variation. The first is the quality of the boron diffusion, and the second is the amount of time the sample spends in the etching solution. Proper cleaning of the Si wafer, a uniformly spun-on boron layer, and accurate control of furnace temperature and gas flow are all necessary to produce a good B diffusion. The correct length of time to leave the sample in the etching solution is the maximum possible without the thin window breaking. If the sample is pulled out too soon, the surface will have excess Si in some places because of the non-uniformity of etching. Cheung, using backscattering analysis, found that the thickness of a sample produced with this method varied by only ±60 Å out of 1600 Å (~4%) [Che80].

In general, we find that a good thin window has less than 10% thickness variation. To study the effect of length of etching time on thickness variation, we prepared two kinds of samples: one that was pulled out of the etching solution early and another that was left in the solution well past the time when the island of Si in the middle of the thin window disappeared. The samples are thin enough to be translucent and to display interference fringes due to light reflecting from the front and back surfaces. The sample removed early indeed demonstrated enhanced thickness variation and the one left longer appeared relatively flat, based on the visible interference fringes.

We then studied these two samples with ion scattering, and the results are shown in Figure 4-12 and Figure 4-13. The spectra shown are taken from the two transmission detectors, and only enough of each spectrum is shown to highlight the high energy side of the Si peak. The position of this side of the Si peak on the energy axis is a function of the Si thickness because the ions that contribute to this part of the peak have scattered from the back side of the sample (discussed earlier in this chapter; see Figure 4-5). The spectra were collected on several different spots on the thin window and for <100>, {100}, {110}, and random beam incidences. From the 150° detector, we found that the sample of Figure 4-12 varied in thickness from 4700 Å to 5300 Å, whereas the sample of Figure 4-13 varied from 4500 Å to 7000 Å. The important (and expected) result here is

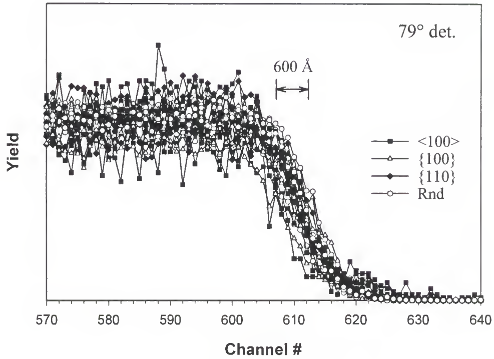

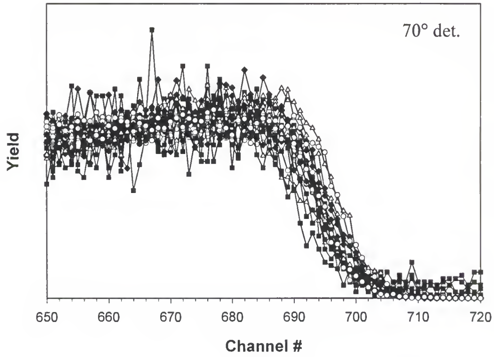

Figure 4-12. Si peaks from spectra taken on sample with little thickness variation. (Random and planar spectra have been scaled for easy comparison of Si half-heights.)

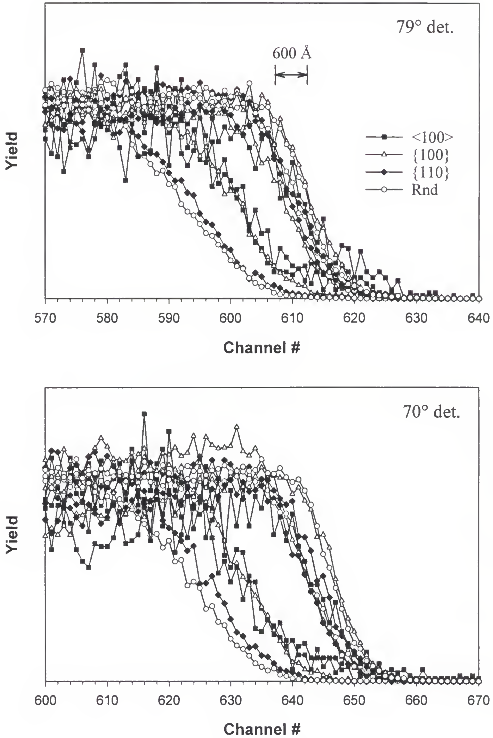

Figure 4-13. Si peaks from spectra taken on sample with great thickness variation. (Random and planar spectra have been scaled for easy comparison of Si half-heights.)

that the Si position varies much less for the sample that showed visual evidence of little thickness variation than for the one that showed evidence of great thickness variation.

The original reason for undertaking this study was to elucidate an anomalous trend in our data, namely a shift in the Si position for spectra at different beam incidences on the same spot on the sample. Often in going from the <100> direction to the planar and random directions, the Si peak shifts to higher energy. An example of a large shift in Si position between <100> and random spectra is shown in Figure 4-14(a) and (c). Again spectra from both transmission detectors are shown with the shift appearing in both of them. Figure 4-14(b) and (d) show the positions of the Si peaks for the same directions but taken on a spot 2 mm away from where the other data were collected, but here there is no shift. The only difference between the two sets of data is the position on the sample.

In Figure 4-14, Figure 4-15, and several similar figures in Chapter 5, the different sets of data have been separated from each other by leaving the left-most data set at the same channel numbers as in the original spectra and shifting the other data sets to higher channel numbers. The only comparison that is being made in these graphs is between the Si half-heights (or Sb peaks) within a particular data set. Comparison of one data set with another is not valid.

Obviously, the 6° sample tilt cannot account for this shift because it would result in a longer path length (by 1/cos6°) through Si for the random direction, as the <100> direction is parallel to the sample normal. What we see instead is that the ions incident in the <100> direction appear to have traveled through a much greater thickness than those incident in the random direction for the two spectra on the left.

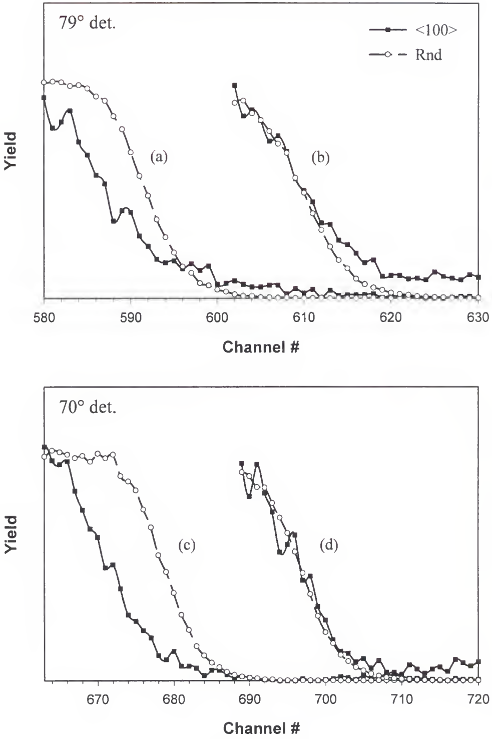

Figure 4-14. Si peak shifts for two spots on the same sample. (Random spectra have been scaled for easy comparison of Si half-heights, and data sets (b) and (d) have been shifted to higher channel numbers.)

In the energy distribution analysis presented in Chapter 5, we deal with Ge and Sb peaks, which result from ions scattering after having passed through the Si. If the shift in Si position indeed indicates thickness variation, then we would expect to see a shift in the Ge and Sb peaks as well. The reason for this stems from the ion beam being composed of channeled and dechanneled ions. The He^+ ions that contribute to the Si peaks are those that have been dechanneled, whereas the ions that scatter from Sb (in dimer sites) are from the channeled portion of the beam. If thickness variation is responsible, then both portions should show greater energy loss, and thus the Sb peak would shift to lower energy also. If only one portion of the beam shows greater energy loss, then some other mechanism must be responsible.

Figure 4-15 shows the Sb peaks corresponding to the Si peaks of Figure 4-14, and a shift can be seen clearly. In Figure 4-15(a) and (c), the Sb peaks for axial incidence are nearly at the same position on the energy axis as the Sb peaks for random incidence. In Figure 4-15(b) and (d), however, the axial peaks are well separated from the random peaks. These relative positions exactly correspond with the shifts seen in the Si peaks in Figure 4-14. Therefore, both the channeled and dechanneled ions show enhanced energy loss.

One potential pitfall here is that the position of the Sb peak for all but the random spectrum could show a shift due to different Sb sites. That possibility is minimal for the data shown in Figure 4-15 because the only difference between the two spectra was the position on the sample. (The two spots were only 2 mm from each other.) The peaks are not from different samples, and the sample was not annealed between the two sets of data. These data provide clear evidence of thickness variation.

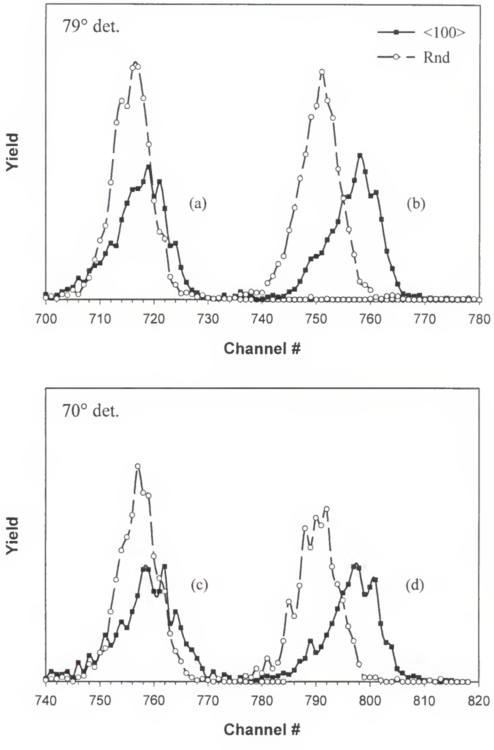

Figure 4-15. Sb peaks corresponding to the spectra of Figure 4-14. (The peaks in (b) and (d) have been shifted to higher channel numbers.)

When we determine the Si thickness from the random spectrum and then find that the axial or planar spectra taken on the same spot show evidence of having a different thickness, we use the position of the Si peak to determine the thickness of those spectra. To do this, we find the channel number of the high energy side of the Si peak for each spectrum, calculate the energy with the energy calibration parameters, and then use the empirical energy loss data [Zie77] to find the thickness, as we did with the 150° detector random spectrum. We then use that thickness in our Monte Carlo simulation for that direction rather than the thickness obtained from the random spectrum.

An important question that has not been answered yet concerns why we should see thickness variation at all if we are taking spectra on the same spot on the sample. The answer is that when we tilt and rotate the sample by changing A and C on the goniometer, the beam does not always hit the same spot. Evidence of this can be seen on the beam spots visible on a used sample. Although the beam covers only 1x1 mm^2, used samples show beam spots smeared out to two or three times that area.

Another means of checking the thickness variation on a sample is to look at a plot of the Ge and Sb peaks in the random spectra taken on different spots. Such a graph is shown in Figure 4-16 for a sample with little thickness variation and another in Figure 4-17 for a sample in which one of the spots appears thicker than the other three. Occasionally, a shift in the Si peaks for different spectra on the same spot indicates a greater thickness variation on that one spot than a plot of the random peaks indicates over the whole sample. In such cases, the discrepancy points to other causes of the shift in Si peaks.

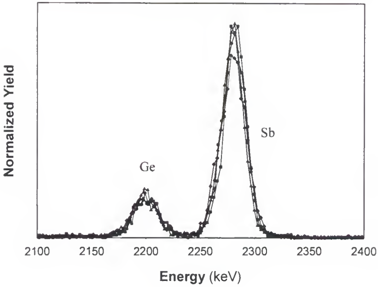

Figure 4-16. Overlapping experimental energy distributions for random incidence showing evidence of little thickness variation.

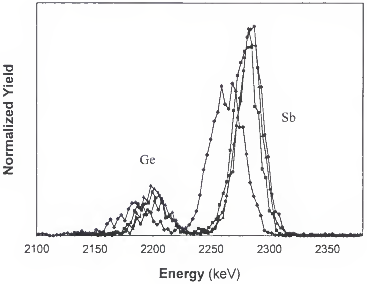

Figure 4-17. Overlapping experimental energy distributions for random incidence showing evidence of one spot having greater Si thickness than the other three.

CHAPTER 5
SURFACE STRUCTURE DURING SURFACTANT-MEDIATED EPITAXIAL GROWTH OF GE ON SI(100)

With the power and limitations of our surface characterization technique revealed (Chapter 4), let us now describe our work in the epitaxial growth of Ge on Si(100). We have studied a method, called surfactant-mediated epitaxy, that can change the way that Ge grows on Si and Si on Ge. By the introduction of a third species, a "surfactant", this method allows for the fabrication of Si-Ge superlattices with sharp, flat interfaces.

We begin the chapter with a look at the relevant background material, that is, details about epitaxial growth, how a surfactant modifies the growth process, and what is known about surfactant-mediated growth. The experimental procedures common to all the work in this chapter then are presented. Finally, we give the results of our study of this problem. The first section is an extension of our previous analysis to a new exchange model. The second part presents new data on this system with a high (2 ML) Ge coverage. The final section contains the results and discussion of our work on an intermediate Ge coverage (0.4 ML), with special attention given to an issue that hampered our ability to make an accurate determination of the surface structure.

Background

Studying surface structure to learn about surfactant-mediated epitaxial growth of Ge on Si(100) with Sb as a surfactant requires knowledge of several important topics. The nature of the Si(100)-2x1 surface is the natural starting point, followed by the structure of the Sb-covered Si(100) surface. As a prelude to surfactant-mediated epitaxy, we will look at what is known about epitaxial growth, including the different growth modes and their thermodynamic causes. The final part of this section will examine the issues of surfactant-mediated epitaxy and the details of the exchange models that have been proposed.

The Si(100) Surface and Epitaxial Growth

Schlier and Farnsworth were the first to study the structure of the clean Si(100) surface. They observed a 2x1 LEED pattern and proposed that this pattern resulted from the reconstruction of top layer atoms to form rows of dimers [Schl59]. After three decades of debate about the nature of these dimers, they are now generally believed to be asymmetric and buckled, with the two Si atoms rapidly oscillating between the up and down positions [Dab92]. The elucidation of the surface reconstruction took such a long time because calculations showed only a slight energy difference between symmetric and asymmetric dimers [Red82, Dab92] and because STM studies saw the rapidly oscillating buckled dimers averaged out as symmetric dimers [Dab92]. The keys to understanding the dimer geometry came from STM observations of buckled dimers near defects [Hame86] and an increase in the number of buckled dimers as the sample temperature decreased [Wol92].

This dimerized surface, then, is the starting point for studies of epitaxial growth on Si(100). In the experiments described in this chapter, we deposited Sb onto this surface and then Ge onto the Sb/Si(100) system. The structure of Sb on Si(100) is well understood. The Sb breaks the Si dimers [Cao92, Sli92], saturates at a coverage of ~0.85 ML when deposited at an elevated temperature [Bar86], and forms symmetric dimers with a dimer bond length of 2.8 Å [Gra92, Ric90]. Furthermore, because of the 12% lattice mismatch between Sb and Si, the Sb dimers cover the surface in short strings that exhibit many antiphase domain boundaries [Ric90, Nog91]. The Sb-terminated Si(100) surface also differs from that of Si(100) by the substitution of lone pair orbitals for dangling bonds because of Sb's five valence electrons, thus passivating the surface [Tan93].

Epitaxial growth on Si(100), or any other surface, generally occurs in one of three modes. One possibility is that the overlayer can grow on top of the substrate one layer at a time, maintaining a flat profile as the overlayer develops. At the other extreme, the overlayer can coalesce on top of the substrate, forming three dimensional islands. The third form of growth combines the features of the first two: the overlayer grows layer by layer to a thickness d_{SK} at first and then develops three dimensional islands. These three growth modes are called Frank-van der Merwe (FM), Volmer-Weber (VW), and Stranski-Krastanov (SK), after the investigators who first described them [Zan88], and are depicted in Figure 5-1.

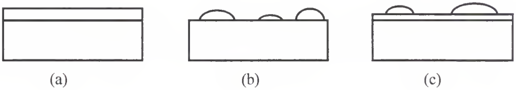

Figure 5-1. Three modes of epitaxial growth. a) Frank-van der Merwe (FM); b) Volmer-Weber (VW); c) Stranski-Krastanov (SK) .

In addition to these three growth modes, other characteristics also can play a large role in the structure of overlayers. As mentioned above, d_{SK} is the thickness when islands start to form on the surface, generally to relieve strain. The formation of islands, however, does not imply the introduction of defects. The thickness at which the first defects appear is defined as the critical thickness, d_{crit}, which can be different from d_{SK}. Islands may begin to relieve the strain in the overlayer, but they still can be coherent with the substrate and defect-free [Tou93]. Another important quality of overlayers is pseudomorphy, when the film adopts the in-plane crystal structure and lattice parameter of the substrate, although different from its own [Zan88]. Ge grows pseudomorphically on Si to a thickness of about 4 ML [Asa85], and has a critical thickness, d_{crit}, of about 6 ML [Bev86].

Those who fabricate bicrystalline structures need to know more than just the description of the three growth modes, however. They also need information about the conditions under which each of the three modes can be observed. By appealing to the surface free energies involved, we can provide an adequate account of what causes a particular system to adopt one growth mode over another. To do so, we relate the surface free energies of the substrate (σ_s), interface (σ_i), and overlayer (σ_o) by comparing the net surface free energies of the FM and VW modes [Zan88]. The results can be summarized by the following relations:

$\sigma_o + \sigma_i < \sigma_s$ layer by layer (FM)

$\sigma_o + \sigma_i > \sigma_s$ 3D islands (VW)

$\sigma_o + \sigma_i \approx \sigma_s$ layer by layer followed by islands (SK)

It is important to point out here that, although these relations generally yield good predictions for the type of growth a system will display, they do not provide a complete description of the driving forces involved. Two issues ignored here are, for example, anisotropy of the surface tension and the difficulty of choosing a value for σ_i. Moreover, these relations are based on the macroscopic surface free energy (or, equivalently, the surface tension), and epitaxial growth is a distinctly microscopic phenomenon.

The above relations place an obstacle in the way of the fabrication of superlattices. Since σ_i is generally small (at least initially), the relation between σ_o and σ_s primarily determines the growth mode. If the overlayer grows in the layer by layer mode in one section of the superlattice, then the next section naturally will grow in the islanding mode, as the material that was the substrate is now the overlayer, and the surface free energy relation is reversed.

For the case of Si and Ge, the surface free energy of Ge is lower than that of Si. Therefore, Ge initially grows layer by layer on Si but, because of the 4.2% lattice mismatch and the resulting strain, starts to form islands at ~4 ML. The growth mode is therefore SK [Asa85]. When Si grows on Ge, on the other hand, islands form immediately, and the growth mode is VW [Asa85]. Further, Ge's lower surface free energy leads to intermixing when Si is grown on top of it [Iye89]. These constraints indicate that a Si-Ge superlattice grown by conventional MBE methods will have interfaces of poor quality, and thus will exhibit less than optimal electronic properties. Three dimensional islands can be restricted kinetically by reducing the sample temperature or increasing the growth rate but only at the expense of the crystallinity [Tou93].

Surfactant-Mediated Epitaxy

In 1989, Copel *et al.* devised a clever way to circumvent the thermodynamic restrictions to layer-by-layer growth in superlattice structures [Cop89]. By introducing a carefully chosen third species, a "surfactant", they were able to inhibit the growth of islands on the surface for Ge/Si(100) and Si/Ge/Si(100). Using As as a surfactant (same group as Sb), they studied this method both theoretically and experimentally. First they performed energy minimization calculations using density functional theory and found that As termination of both of the systems mentioned above was highly favored over either Ge or Si termination. They next studied these systems with medium energy ion scattering and discovered that As deposited concurrently with 15 ML Ge resulted in Ge films with minimum yields of less than 5%, indicating good crystallinity. They also found strong evidence for Si islands in Si/Ge/Si(100), whereas prior As deposition produced backscattering spectra indicative of flat layers of Si and Ge. Finally, they showed with x-ray photoelectron spectroscopy that the As continually segregates to the surface during growth at 500° C. This segregation, as will be discussed in greater detail later in this section, means that the surfactant and overlayer atoms exchange positions during growth.

This groundbreaking work led to tremendous effort by numerous research groups to characterize the films grown by and to understand the process of surfactant-mediated epitaxy (SME). (As testament to this, a review article written only four years after the Copel *et al.* paper contains 166 references, although, of course, not all of these are studies of SME [Tou93].) The research in this area covers the application of SME to many different systems (e.g., Si/Ge, III-V compound semiconductors, and Ag/Ag) and the (100), (110), and (111) surfaces. Many different materials have been used as surfactants, and the growth has occurred under a wide range of conditions [Tou93]. As the work presented herein is concerned only with the Si-Ge system on the (100) surface with Sb as a surfactant, we will discuss primarily the research results relevant to those conditions.

Before plunging into the details of what makes SME work, let us first examine some of the characterization results. One of the most striking changes is that the surfactant extends the pseudomorphic region in a Ge overlayer on Si(100) from ~4 ML to ~12 ML [Leg89] and increases the thickness for complete strain relaxation from ~10 ML to ~60 ML [Tho91]. Moreover, the strain is relieved in this case via a "V-shaped" defect [Leg89, Koh92] rather than a misfit dislocation. In the pseudomorphic region, Horn-von Hoegen *et al.* [Hor94a] found that the surface was roughened with circular cone-shaped Ge islands when growth occurred at 700° C and was even rougher at 300° C. They explain this enhanced roughness as a means of strain-relief before the introduction of defects. Upon further Ge deposition, the defects relieve the strain and then the film can grow with a smooth, flat surface. In the case of Ge δ layers (~1 ML) covered with a Si cap, Falta *et al.* found that SME produced the smallest interface roughness and highest Ge concentration in a comparison with conventional MBE and solid phase epitaxy [Fal96].

A critical issue in SME is the amount and effect of surfactant that remains in the films. Horn-von Hoegen *et al.* state that the concentration can be as high as 10^{19} cm^{-3} [Hor94b]. This is clearly high enough to impact the electronic properties when the surfactant is a dopant, as Sb and As are. In fact, not only are these the most often used surfactants, but they are also both n-type dopants, and p-type surfactants have not produced high quality films through SME [Tou93]. Recent results, however, have suggested a way around this problem. Through high temperature (720° C) SME, Reinking *et al.* were able to reduce the Sb concentration in 1000 nm Ge films grown on Si(111) to the 10^{16} cm^{-3} level and also improve the electronic transport properties [Rei97]. Similarly for 3 ML Ge films, De Padova *et al.* have shown that post-growth annealing cycles at 750° C allow for the complete removal of the Sb and recovery of the Ge/Si(100)-2x1 surface [Dep98].

Whereas the characterization of SME-grown samples generally has resulted in increased understanding of these materials, the effort to comprehend the process of SME itself still has not resolved the fundamental questions. A few of these open questions are: (i) Does the change in growth mode occur for thermodynamic or kinetic reasons? (ii) Is diffusion of overlayer atoms enhanced or reduced on the surfactant-covered surface? (iii) What are good surfactants? (iv) What are the details of the exchange process when the surfactant segregates to the surface during growth?

Beginning with Copel *et al.*, the change in growth mode has been ascribed to kinetics by nearly all researchers in this area [Cop89, Tou93]. A reduction in the surface free energy is the driving force for surfactant segregation, but, it is thought, the kinetic details control the type of growth obtained. The general description that evolved had Ge deposited on the surfactant-covered surface and quickly incorporated into the film by exchange with the surfactant [Tou93]. The rapid exchange caused reduced diffusion of Ge on the surface, thus preventing the growth of three dimensional islands.

The first evidence for reduced diffusion is the work of Tromp and Reuter, who found that a surfactant changed the growth pattern from step-flow to the nucleation of numerous small two dimensional islands [Tro92]. They reasoned that this change must be due to reduced diffusion. Another claim for reduced diffusion came from Voigtländer *et* *al.* [Voi95]. They looked at the influence of group III elements Ga and In and group V elements As and Sb on the homoepitaxy of Si on Si(111) and asserted that the group III elements enhance diffusion whereas group V elements reduce diffusion. Their evidence for this came from the island density in the presence of the impurity relative to the island density for pure Si homoepitaxy. In other words, their claim for reduced diffusion of As and Sb is the same as that made by Tromp and Reuter.

In contrast, Kandel and Kaxiras have pointed out that the argument for reduced diffusion is flawed because it requires the energy barriers for exchange and diffusion to be comparable [Kan95]. Diffusion on the passivated surface, they say, should occur much more easily than the interlayer exchange with its consequent breaking of chemical bonds. In an attempt to find a lower bound for these energy barriers, Kandel and Kaxiras performed first-principles quantum mechanical calculations for these processes and found that the diffusion barrier is about half of the exchange barrier. They claim that diffusion is enhanced for SME on semiconductors, but the mechanism for layer-by-layer growth is still kinetic and is determined by bonding at the step edges.

Returning to the issue of kinetics versus thermodynamics, we find some interesting studies that point toward thermodynamic causes. For example, Osten *et al.* discovered that a smooth, flat film resulted whether deposition of the surfactant occurred before or after Ge deposition [Ost92]. For the latter case, they created 10 nm and 30 nm amorphous layers of Ge grown at room temperature, capped them with Sb, and then annealed the system. Likewise, Eaglesham *et al.* studied the resulting equilibrium island shape of Ge on Si(100) upon post-growth anneals in a flux of Sb, In, or H [Eag93]. Because the equilibrium island shape depends on the surface energy anisotropy, they claim that this thermodynamic quantity plays a significant role in SME. More recently, Jenkins and Srivastava point directly to thermodynamic grounds for surfactant behavior and state that modification of the chemical potential is the crucial issue [Jen98].

These results certainly raise the questions of just what a surfactant is and what makes a good surfactant. A conventional surfactant is defined as a substance that lowers the surface tension of a liquid and enhances its wetting properties [Isa96]. In SME, that definition would imply that only those species that both segregate and induce layer-by-layer growth are surfactants and that the driving force is thermodynamic. The trend in this field, however, has been to label any species that lowers the surface free energy as a surfactant, regardless of the accompanying growth mode [Cop89, Voi95]. For consistency, then, we also will follow this trend.

According to Voigtländer *et al.*, a good surfactant is one that inhibits island growth by reducing the adatom diffusion [Voi95]. As mentioned above, however, the evidence for reduced or enhanced diffusion is indirect and in dispute. What we can say is that a good surfactant promotes layer-by-layer growth, and thus As and Sb are good surfactants. They do have the drawback of doping the film, but non-doping surfactants like Pb and Sn, do not inhibit three dimensional island growth [Hib94, Lin95]. In contrast to As, Sb is much less volatile and has been shown to be more effective in inhibiting islands [Hor94c]. (For our ion scattering experiments, Sb has another advantage: The difference in mass between it and Ge is much larger than between As and Ge, providing greater separation between the Ge and Sb peaks.) Tersoff *et al.* give another criterion for a good surfactant. They state that the important function of a good surfactant is to nucleate two dimensional islands close enough to one another that they coalesce before reaching the critical size for three dimensional growth [Ter94].

This lack of clarity about what causes SME, then, prefaces our effort to understand the exchange mechanism during segregation of the surfactant. As with the other issues in SME, the causes of segregation and the exchange mechanism remain vague. Three models for the exchange mechanism have been proposed, but little experimental work has been done in this area. Let us now look at these models, which, for brevity, will be referred to as the Tromp, Yu, and Ko models. (In the descriptions that follow, we will use Sb as our surfactant although the three studies in question used As.)

The first attempt to explain the exchange process between surfactant and adsorbate atoms was the two-dimer correlated exchange model of Tromp and Reuter [Tro92]. Based on their aforementioned observation of many small two dimensional islands on the surface and the counting of dangling bonds, they proposed that Ge first will adsorb onto the Sb-terminated Si(100) surface (Figure 5-2(a)) by breaking the Sb dimers and forming Ge dimers rotated 90° to the Sb dimers (Figure 5-2(b)). The exchange of one Ge dimer with underlying Sb results in no reduction in dangling bonds on the surface, but two dimers exchanging together decrease the number of dangling bonds by four. The exchange puts Ge in near-substitutional sites beneath Sb dimers, an atomic configuration that we call the "final state" (Figure 5-2(c)). Further growth then proceeds one Ge dimer at a time with the original exchange acting as a seed for needle-like growth. (Ohno suggested a similar process two years later [Ohn94].)

The second major model came out in 1994 and was the work of Yu and Oshiyama, who based their proposed segregation path on total energy calculations

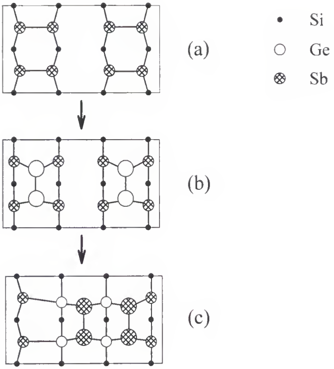

Figure 5-2. The Tromp model. a) Sb-terminated Si(100) surface; b) Ge dimers on substitutional Sb; c) the final state, Sb dimers on top of near substitutional Ge. (Size of circle indicates proximity to surface, with largest being in top layer.)

[Yu94b]. Unlike Tromp and Reuter, however, they found that the Ge adatoms prefer to adsorb between the Sb dimer rows without breaking the Sb dimers (Figure 5-3(b)). They also found it energetically favorable for a single Ge dimer in that position to exchange with underlying Sb. The result of this exchange is Ge in heterodimers with Sb beneath a dimer with Sb atoms in near-interstitial sites (Figure 5-3(c)). This construction modifies the surface energy enough that additional Ge adatoms can break the neighboring Sb dimer and form a rotated Ge dimer next to the near-interstitial Sb dimer (Figure 5-3(d)). From this configuration, exchange to the final state (Figure 5-3(e)) occurs readily, with further growth ensuing in needle-like fashion, as in the Tromp model.

Continuing the trend of reducing the size of the exchanging unit, the third model is called the single adatom exchange model and was proposed by Ko *et al.* in 1996 [Ko96]. (In contrast to the other models, they studied the case of Si homoepitaxy, but the results should be applicable to Ge/Si also.) This model also results from total energy calculations and is marked by a single Si atom adsorbing between the Sb dimer rows and exchanging immediately with an underlying Sb atom. This exchange creates an Sb atom lifted above a Si- Sb heterodimer and sitting in a substitutional site (Figure 5-4(b)). As more Si adsorbs, another single adatom exchange will eventually occur next to the original one (Figure 5-4(c)). The two lifted Sb atoms can then dimerize and move to the same near-interstitial sites that Yu and Oshiyama found (Figure 5-4(d)). This protruded Sb dimer acts as a seed for further growth, which leads to the final state (Figure 5-4(e)) and then needle-like growth.

Experimental work to clarify the exchange process has been sparse. Yu *et al.* claimed to have found Ge dimers adsorbed between As dimers rows in an STM study of this system, although their evidence consisted of only one image showing two islands that they asserted to be Ge dimers [Yu94a]. Their finding, if accurate, lends support to the Yu model. Earlier work in our lab also seems to endorse a modified version of the Yu model. We found that after room temperature deposition of Ge on Sb-terminated Si(100), the Ge occupies dimer-like sites having a longer dimer bond length than Ge dimers on Si(100), and the Sb appears to be in undisturbed dimer sites [Bos96b]. (Although not an experimental study, recent work by Jenkins and Srivastava also found elongated Ge dimers for this system, but they appeared on top of broken Sb dimers [Jen97b].) After annealing the sample at 350° C, we found the system to be in the final state. Using a

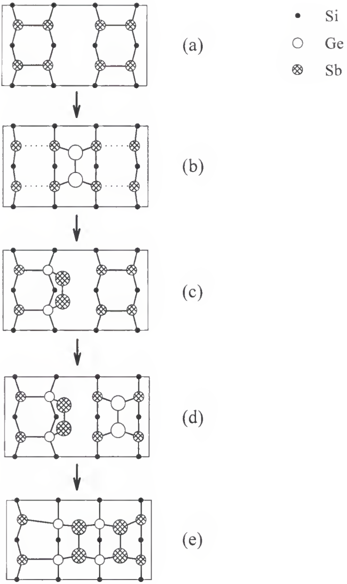

Figure 5-3. The Yu model. a) Sb-terminated Si(100) surface; b) Ge dimers between Sb dimer rows; c) protruding Sb dimer after single dimer exchange; d) protruding Sb dimer with neighboring Ge dimer; e) the final state, Sb dimers on top of near substitutional Ge. (Size of circle indicates proximity to surface, with largest being in top layer.)

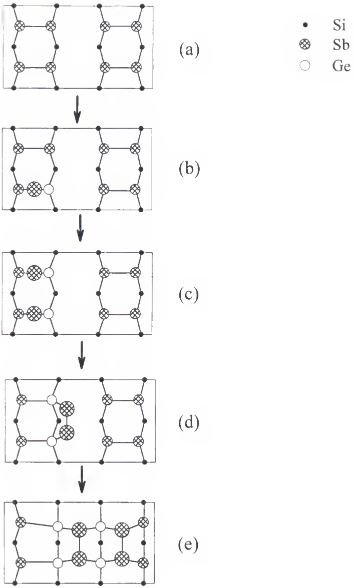

Figure 5-4. The Ko model. a) Sb-terminated Si(100) surface; b) lifted Sb atom after single adatom exchange; c) two lifted Sb atoms after single adatom exchanges; d) protruding Sb dimer; e) the final state, Sb dimers on top of near substitutional Ge. (Size of circle indicates proximity to surface, with largest being in top layer.)

similar room temperature deposition, Cao *et al.* found the Ge to be disordered before annealing [Cao92]. Their paper does not report the Ge coverage, but it seems that they deposited a thick layer (nanometer range), hence the disorder.

Certainly the most puzzling experimental result of the few that exist is the work by Ide [Ide95]. In an STM study of this system with As as a surfactant, he found that Ge depositions at 300° C, 400° C and 500° C produced remarkable results. At 300° C the two dimensional islands on the surface run *parallel* to the underlying As dimer rows. At 500° C, on the other hand, the islands have transformed to run perpendicular to the underlying dimers. At 400° C a mix of parallel and perpendicular was observed. He did confirm that the growth is needle-like, as both kinds of islands that he observed appear to be only one dimer wide.

Ide states that Auger electron spectroscopy (AES) data indicate that segregation has already occurred at 300° C, and hence the parallel islands consist of As atoms. AES, however, is not well suited to distinguishing between first and second layer As, and his STM images were obtained at submonolayer Ge coverage whereas the AES study was done after further Ge deposition to a coverage of 10 ML. Nevertheless, whether the parallel islands are Ge or As, none of the models proposed contains any mechanism for this kind of growth. Indeed, even attempting to explain these structures outside of the boundaries of SME is difficult.

Experiment

The experiments described in this chapter all followed the same procedure. The main steps were to: (1) desorb the oxide, (2) deposit ~0.85 ML Sb at 500° C, (3) deposit

0.15 to 2.0 ML Ge at RT, (4) collect ion scattering data, (5) anneal the sample at a temperature from 80° C to 500° C, and (6) repeat step 4. The principal differences between experiments were the Ge coverage and the annealing temperature. Additional variation lay in the use of a new thin window for each experiment and the choice of which planar spectra to collect data for. (In the earlier experiments, we often looked only at {100} or at {110} beam incidence, although later we did both.)

Each experiment began with the Shiraki oxide desorption, after which LEED yielded a two-domain 2x1 pattern with low background and sharp spots, indicating a properly prepared Si(100) surface. Next we deposited Sb from a boron nitride effusion cell with the sample heated to ~500° C. Exposure of the sample to several monolayers of Sb ensured saturation at ~0.85 ML [Bar86]. The LEED pattern at this point changed to 1x1 with faint half-order spots.

After allowing the sample to cool to near room temperature, we deposited Ge from an effusion cell at the rate of 0.15 ML/min. No noticeable change occurred in the LEED pattern for samples with low Ge coverage (~0.15 ML), whereas the samples with moderate or high Ge coverage (0.4-2 ML) showed a LEED pattern with higher background and half-order spots weaker or no longer visible. The Sb and Ge coverages were determined to within ±10% with the use of Rutherford backscattering (RBS) analysis. More detailed descriptions of our sample preparation procedures and experimental setup can be found in Chapter 2.

Upon completing the sample preparation, we transferred the sample under UHV to the scattering chamber and placed it on the goniometer. The 2.5 MeV He^+ beam, collimated to an angular divergence of 0.03°, then was steered into the scattering chamber. With the sample in transmission geometry (adsorbates on the beam-exit side of the sample), we visually aligned the <100> axis of the sample with the beam by viewing the transmitted beam on the quartz at the end of the beamline. Taking as a second reference point a beam incidence ~8° from the <100> axis along the {100} plane, we established the relation between lab and crystal coordinates [Dyg93]. Thus we could readily choose a beam incidence at any tilt θ from the <100> axis and azimuth φ relative to the {100} plane.

In these experiments, we obtained energy distributions in three directions: (θ,φ) = (0°,0°), (6°,0°), and (6°,30°). The first of these directions is the <100> axis, the second is the {100} plane, and the third is a "random" direction, in which ion energy losses approach those in amorphous media [Zie77]. The direction chosen as the random was based on simulating mean ion energy loss over a large range of θ and φ and finding a direction where the difference between mean energy loss and random energy loss was minimal [Bos95b, Bos96a]. Data taken in the experiments consist of the three spectra at different beam incidences, after room temperature Ge deposition (henceforth called "before anneal") and again after annealing the sample at temperatures from 80° C to 500° C for 10 minutes each.

The integrated beam current of each spectrum was limited to a maximum of 48 μC (3×10^{16} ions cm^{-2}) for the <100> direction and 32 μC (2×10^{16} ions cm^{-2}) for the {100} and random directions. These doses are within the range of beam dose that yield acceptable levels of irradiation damage to the Si crystal structure [Fel82]. Furthermore, the spectra were generally collected 16 μC at a time to monitor the Si yield for evidence of excessive damage. Likewise, we collected the axial and planar incidence data before the random incidence data because of the greater damage caused by the random incidence beam. One more step taken to minimize crystal damage was collecting pre- and post-anneal data on different spots on the thin window. The three spectra (<100>, {100}, and random) corresponding to a given temperature and Ge coverage were taken on a single spot, however, in order to minimize problems with variations in adsorbate coverage and Si thickness.

Results and Discussion

The work presented in the following sections was undertaken to learn more about the details of surfactant-mediated epitaxy. First we look at how a new exchange model compares to data that we used to study the two previously-published models. We used the same data here that we obtained for the earlier study so that the three models all would have been tested against the same data. The high Ge coverage experiment was an extension of the previous work to study the effect of coverage and the transition to the final state. In the last section, we present our work with a Ge coverage of ~0.4 ML and annealing at several different temperature. The goal here was to follow the segregation of the Sb and learn about its temperature dependence. Unfortunately, we found that unexpected energy loss mainly in the <100> direction created difficulty in making an accurate determination of the surface structure.

The Single-Adatom Exchange Model and Previous Data

In this section, we compare our previously-published experimental transmission ion channeling data [Bos96b] to the single-adatom exchange model [Ko96]. (The analysis presented here was published in the work by Bailes *et al.* [Bai98a].) Ko *et al.* state that under the proper conditions (low growth temperature and low adatom coverage), an intermediate state with a surfactant atom residing directly above a surfactant-adsorbate heterodimer should be observable. We have found, however, that this configuration of surfactant and adsorbate atoms does not fit data we have collected after sample preparation under the specified conditions, nor does it fit our data taken after annealing the sample at 350° C or using a higher Ge coverage.

Comparing our data to other stages of the single-adatom exchange model was unnecessary for two reasons. First, we have tested the state that Ko *et al.* specify as the one that we should see for our sample preparation conditions. Second, the other states we could test are similar to parts of the Yu and Oshiyama model that we have tested previously [Bos96b]. Along with the comparison of our data to the Ko model, we show comparisons to the final state and to the state which best fits the data, Ge in dimer-like sites on top of undisturbed Sb dimers.

Before discussing the data and simulations, we need to clarify exactly what adatom sites we have tested in each of the simulations. Figure 5-5 shows top views of the three states we tested. The intermediate state of the Ko model, with an Sb atom on top of an Sb-Ge heterodimer, is shown in Figure 5-5(a). We took the Sb atom on top to be in a substitutional site; however, moving it up to 0.4 Å away from a substitutional site does not change the result significantly. The Sb dimers have the experimentally measured dimer bond length of 2.80 Å [Bos95b, Gra92], and we treated the Sb-Ge heterodimers as if each atom were in a homodimer. Thus, the Sb atom is in the same site as the other Sb dimer atoms on the surface, and the Ge atom is in a site that would give it the experimentally measured dimer bond length of 2.60 Å if it were part of a Ge-Ge dimer

[Gra94c]. Since this is the only part of the Ko model that we tested, from this point forward use of the term Ko model will refer specifically to this state.

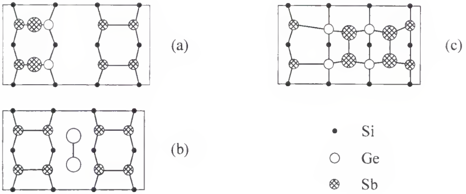

Figure 5-5. Top view of the Si(100) surface showing the three adatom configurations tested. a) Ko model; b) all dimer model; c) experimentally-determined final state. (Size of circle indicates proximity to surface, with largest being in top layer.)

The final state, shown in Figure 5-5(b), consists of Sb dimers on top of near-substitutional Ge atoms, and we have used the experimentally-measured values for the adatom sites [Bos96c, Gra94b]. The last model, shown in Figure 5-5(c), is the configuration we found to fit the before anneal, 0.68 ML Ge data [Bos96b]. We refer to this model, with Ge in dimer-like sites between the Sb dimer rows and Sb in symmetric dimer sites, as the all dimer model. The Sb dimer atoms are in the same sites as in the Ko model, with a dimer bond length of 2.80 Å, and the Ge atoms are in sites identical to the Sb atoms except for a 90° rotation, giving them a 2.80 Å dimer bond length as well.

With these adatom sites for the three configurations, we compared our experimental energy distributions to simulated distributions for beam incidences in the <100> axial direction and along the {100} plane 6° from the <100> axis. We chose these directions because beam incidences near the <100> axis yield the greatest sensitivity to lateral positions on the (100) surface. Simulations showed that other beam incidences near the <100> axis would not add appreciably to our ability to distinguish between models. In fact, in this case the {100} planar incidence data were redundant and therefore are not shown. Beam incidences near other major axes were not used because of uncertainty in the z (distance above surface) coordinates of the adatoms in the different models. Since the Monte Carlo simulation of channeling gives us a distribution of ion positions and energies, the comparison between simulation and data is based on peak height, shape, and position on the energy axis, with a χ^2 value determining the goodness of fit.

Figure 5-6 shows simulated energy distributions for the three atomic configurations described above compared to experimental data taken for the <100> beam incidence on a sample with 0.15 ML Ge on Sb-terminated Si(100). As mentioned before, it was expected that catching the system in an initial or intermediate state requires both low Ge coverage and deposition temperature. The upper set of data and simulations in Figure 5-6 represents the results of our matching these conditions. Whereas both the all dimer model and the final state fit these data reasonably well, the Ko model obviously does not. Upon annealing at 350° C (lower part of figure), the fits between simulations of the models and experimental data do not change appreciably.

We see no evidence that the Ko model describes the state of the system at this low coverage either after deposition at room temperature or after annealing at 350° C. The possibility exists, however, that the transition to the final state has occurred already at this low coverage. In that case, we can say nothing about the initial states. Another possibility

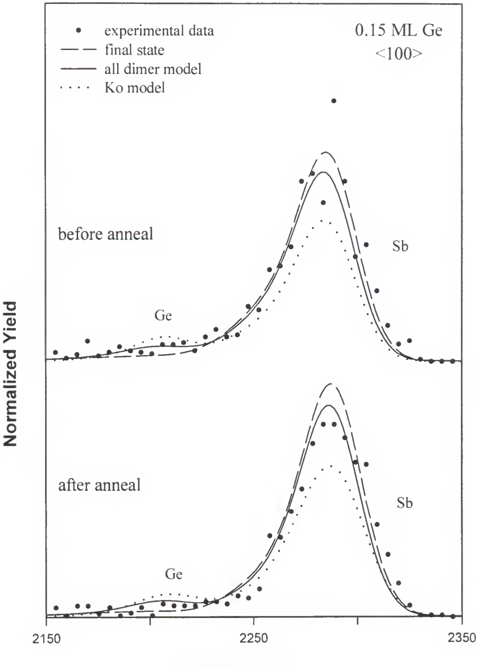

Figure 5-6. Experimental (dots) and simulated (solid, dashed, and dotted curves) energy distributions for the three configurations discussed in the text for 0.15 ML Ge. Slight energy differences in the before and after anneal data arise from differences in Si thickness, as the two sets of data were taken on different spots on the sample.

is that the system is in an initial state such as the all dimer model. The all dimer model and the final state both have Sb in (slightly different) dimer sites, whereas the Ge is in dimer-like sites in the all dimer model and near-substitutional sites in the final state. Thus, distinguishing between these two states requires good statistics in the Ge peak, which we do not have for the low coverage data. Depositing a higher coverage of Ge allowed us to look for a transition induced by annealing the sample, answering the question about whether we can catch the system in an initial state.

Figure 5-7 shows the <100> data and simulations for 0.68 ML Ge on Sb-terminated Si(100) before and after annealing. In this case, the Ge data clearly show a transition from fitting the all dimer model before annealing to fitting the final state after annealing. The Sb data also support a shift from the all dimer model to the final state upon annealing. The Ko model does not fit either the before anneal or after anneal data.

The driving forces that can cause the system to go from an initial state to the final state are thought to be Ge coverage and sample temperature during growth or during subsequent annealing. Since we caught the system prior to the transition to the final state at 0.68 ML Ge before annealing, at the lower coverage of 0.15 ML Ge we also would expect to see the system in an initial state. The inability to discern a transition in the low coverage data could indicate that we had too little Ge on the surface to reach the final state or that the final state is altered by the low coverage and the transition is subtle. From the high coverage scattering yields for the Ge and Sb peaks, we deduced that the all dimer model provides a good fit to the data. If we take the low coverage, before anneal data to be in an initial state, then that state is likely to be the all dimer model and, based on the data, cannot be the Ko model. The Ko model, in fact, fits none of the four data sets.

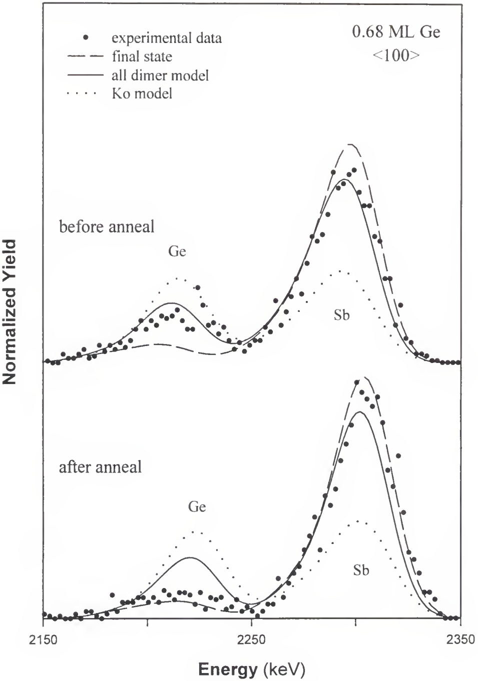

Figure 5-7. Experimental (dots) and simulated (solid, dashed, and dotted curves) energy distributions for the three models discussed in the text for the higher Ge coverage of 0.68 ML.

High Ge Coverage

The preceding section discusses our early work in SME using a low Ge coverage to match the conditions thought necessary for finding the system in an early stage of the exchange process and an intermediate coverage to observe the transition to the final state. Now we discuss an experiment with a still higher Ge coverage, this time 2 ML. This experiment was actually done six months before the 0.68 ML Ge experiment, and the motivation for using this high coverage was the same in both cases. We wanted clear evidence that the system after room temperature deposition was in an initial or intermediate state and that annealing caused a transition to the final state. We also sought to study the impact of Ge coverage on the surface structure before annealing.

The data for this experiment are shown in Figure 5-8 for the sample after room temperature Ge deposition and in Figure 5-9 after the sample had been annealed at 500° C. The energy distributions shown in both cases are those for the <100> and random directions. (We also obtained {110} data but have not included it here because of the problem with planar oscillations that was discussed in Chapter 4.) The experimental data are represented by the dots and the simulations for the final state and all dimer model are displayed as the solid and dashed curves respectively.

The <100> Ge peaks in the before and after annealing data indicate that the system clearly underwent a transition to the final state upon annealing. Focusing on the energy distribution obtained after the anneal (Figure 5-9), we see that the final state simulation fits the Ge peak extremely well and is close to fitting the Sb data. Recall that the final state has near-substitutional Ge beneath asymmetric Sb dimers. In this case, the Sb dimers reside above 2 ML Ge, but the final state configuration was determined for

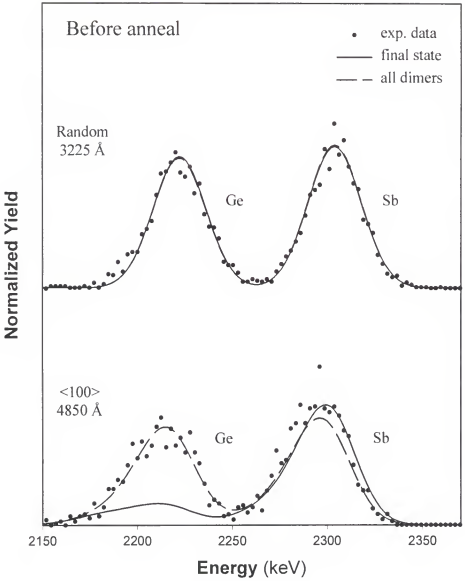

Figure 5-8. Energy distributions after room temperature deposition of 2 ML Ge on Sb/Si(100). (Note that the <100> simulations were based on a greater Si thickness than were the random simulations.)

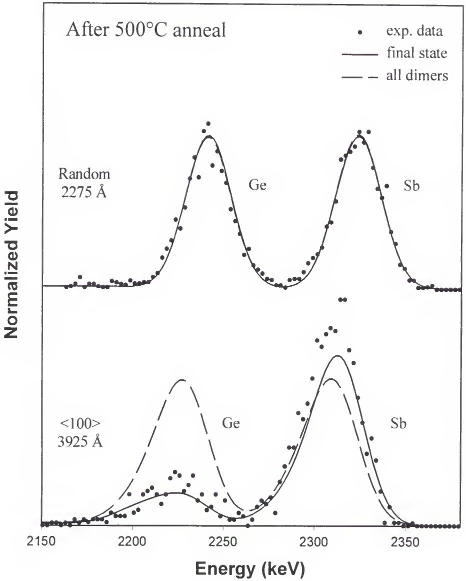

Figure 5-9. Energy distributions after annealing the high Ge coverage sample at 500° C. (Note that the <100> simulations were based on a greater Si thickness than were the random simulations.)

1 ML Ge. The higher Sb yield here probably indicates more disorder in the Sb layer because of the additional (strained) Ge.

Looking at Figure 5-8 again, we see that after the room temperature deposition, the Sb appears to fit the final state better than the all dimer model. This would point to the Sb dimers being slightly disturbed from the symmetric configuration they exhibit on Si(100). The difference between the Sb dimers of the all dimer model and the final state is small however. The major feature of this energy distribution is the Ge peak and its nearly perfect fit to the all dimer model. This fit is surprising because of the high Ge coverage.

An alternative configuration suggested by earlier work is a mixture of pseudomorphic and disordered Ge. Lyman *et al.* studied 1 to 10 ML Ge films deposited at room temperature on Si(100) and claimed that these films were a mixture of up to 50% pseudomorphic Ge with the remainder being disordered [Lym91b]. Accompanying both the pseudomorphic and disordered Ge in their model, however, is a lifting of the Si reconstruction. In our case, the Ge is deposited on the Sb terminated surface, but our before anneal data show no evidence of the Sb dimers being broken. The possibility of pseudomorphic and disordered Ge on top of Sb dimers seems unlikely but cannot be ruled out, nor can the possibility of Sb dimers *on top* of pseudomorphic and disordered Ge, as we have sensitivity only to lateral positions on the surface. The Sb has been found by Cao *et al.* to be buried after RT Ge deposition, however, making the latter possibility unlikely [Cao92]. (A configuration having pseudomorphic and disordered Ge was not tested because of the difficulty of combining well-defined sites with an amorphous component in the site program.)

The Tromp, Yu, and Ko models were not tested here for two reasons: None would yield a good fit to the data, and the proper method of treating the sites is ambiguous. The first assertion can be understood by examining the Sb sites in the models. The Yu model contains interstitial Sb dimers, and the Tromp and Ko models both have substitutional Sb. As can be seen from the fits in the next section, these sites provide characteristic signatures for the different models and would not fit these data for our experiment with high Ge coverage. The second reason stated above is based on the atomic configurations in the models. Figure 5-2, Figure 5-3, and Figure 5-4 show that the ratio of Ge to Sb atoms in these models varies from 1:4 to 2:4. The Ge coverage that would saturate the surface with the Tromp model (Figure 5-2(b)), the Yu model (Figure 5-3(c) or (d)), or the Ko model (Figure 5-4(c)) is half of the Sb coverage, or about 0.4 ML.

Of special note is that the simulations for the <100> data used Monte Carlo generated ion distributions based on greater thicknesses than were found from the random spectra. As indicated in Figure 5-8, the thicknesses for the random and <100> energy distributions were 3225 Å and 4850 Å, respectively, before annealing. Figure 5-9 shows that those numbers were 2275 Å and 3925 Å after annealing. These values for the <100> thickness were determined, as detailed in Chapter 4, by using the shift in the high energy edge of the Si peaks for the <100> and random spectra. Figure 5-10 shows these Si peak edges for the data in this section, and the shift is dramatic.

These variations in thickness for spectra taken near the same spot are even larger than the variation we found between the two spots that we used for the two sets of data. Figure 5-11 displays the two energy distributions for random incidence, the shift indicating different thicknesses on the two spots used. The thickness difference between

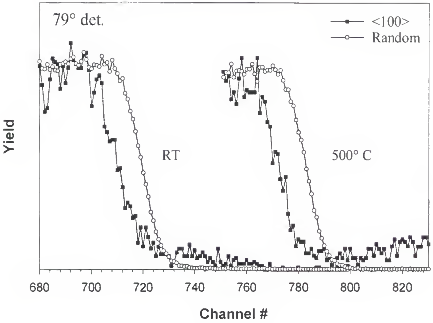

Figure 5-10. Shift between high energy edges of <100> and random Si peaks, indicating what appears to be thickness variation. (Random spectra have been scaled for easy comparison of Si half-heights. Also, the 500° C data have been shifted to the right to separate the two sets of data.)

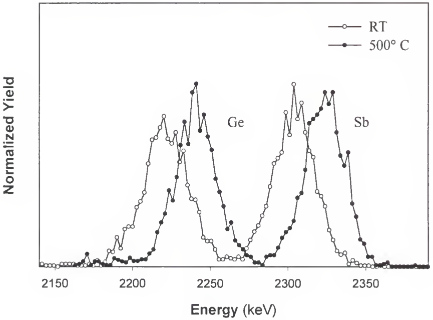

Figure 5-11. Shift between energy distributions for the two random spectra, giving evidence of thickness variation between different spots on the sample.

the two spots, however, was only 1000 Å, whereas between the axial and random spectra on or near the same spot, the difference was ~1600 Å.

Going to Monte Carlo simulations for thicknesses that are 50% and 73% greater in the axial direction than the random is not the ideal way to analyze energy distributions because of the accompanying uncertainty about small shifts in energy. In this case, the simulations appear to fit the data well, but as will be seen in the next section, these thickness adjustments do not always work.

Intermediate Ge Coverage and Incremental Annealing

The next stage of work in our study of surfactant-mediated epitaxy of Ge on Si(100) was to go to a Ge coverage of 0.4 ML and monitor the surface structure at several points in the annealing process. We chose this Ge coverage because it leads to a surface that is fully covered with a particular atomic configuration corresponding to a given model. For example, in the Tromp model, the ratio of Ge to Sb is 1:2. Thus, 0.4 ML of Ge is necessary to combine with 0.8 ML of Sb in saturating the surface with this configuration. Of course, saturation with a particular configuration can occur only if exchange does not take place, and our earlier work led us to believe that this may be the case at RT. By depositing the Ge at room temperature and then annealing the sample gradually, we hoped to be able to observe different phases of the exchange process. We collected ion scattering data after room temperature deposition and after annealing at 80° C, 150° C, 200° C, 350° C, and 500° C.

Before discussing the data, let us review the atomic configurations for which we simulated scattered ion energy distributions. Figure 5-12 shows the six configurations we tested: (a) the experimentally-determined final state, (b) the all dimer model, (c) the

Tromp model, (d) the Yu model, part c, (e) the Yu model, part d, and (f) the Ko model. The previous discussion of the sites used (see the section on the Ko model) applies to these configurations as well. The final state, all dimer model, and Ko model are exactly the same as before. The Ge-Sb heterodimers found in the Yu model were treated as if each atom were in a homodimer. The Tromp model consists of substitutional Sb and dimerized Ge with the dimer bond length that Ge exhibits on the Si(100) surface.

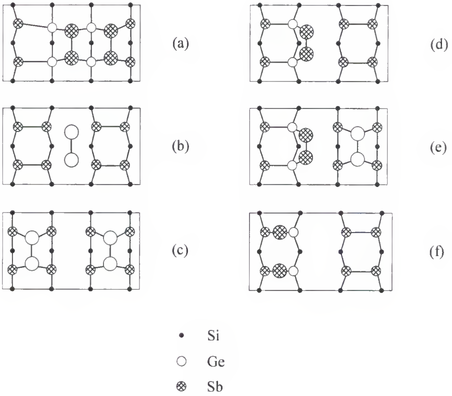

Figure 5-12. Atomic configurations tested. a) final state; b) all dimer model; c) Tromp model; d) Yu model, part c; e) Yu model, part d; f) Ko model.

The experimental and simulated energy distributions are shown in Figure 5-13 to Figure 5-18. The RT and 150° C distributions were obtained from one sample, and the other four sets of distributions were obtained from a different sample. (Because of the time involved and the limited number of spots on the sample, obtaining six sets of data from one sample is not feasible.) The larger dots represent the experimental data, and the solid, dashed, and (smaller) dotted curves depict the simulated distributions.

Some comments about the visibility of the simulations near the Ge peaks are necessary because of the limitations of this form of presentation. First, what appears to be a solid curve lying above the Ge data is actually the overlap of the simulations for the Tromp, Yu, and Ko models and is not the final state simulation. These four simulations (Tromp, Yu c, Yu d, and Ko) overlap because they are all based on Ge dimers with a 2.6 Å bond length. On the other hand, because it has Ge in near-substitutional sites, the final state simulation is the one lowest in yield near the Ge peak for all temperatures. The all dimer model (the smaller dots) lies between the Tromp, Yu, and Ko models and the final state simulation near the Ge peaks. Also, the Yu c simulation is represented by the curve with the longer dashes even though the legend seems to indicate that it is a solid curve.

Looking at the Ge peaks first and focusing only on the relative yields (i.e., neglect energy shifts), we can see a clear trend as the system progresses from the RT deposition to the 500° C anneal. In the RT (Figure 5-13) and 80° C (Figure 5-14) distributions, the <100> axial data fit the all dimer model very well, and the 80° C {100} planar data also appear to fit this configuration. The RT planar data appear to fit the final state, but because the 80° C, 150° C (Figure 5-15), and 200° C (Figure 5-16) planar data have higher yields, there may be a problem with the experimental yield in the RT data.

In the 150° C and 200° C axial and planar Ge peaks, the data are at an intermediate state between the all dimer and final state simulations. In the 350° C

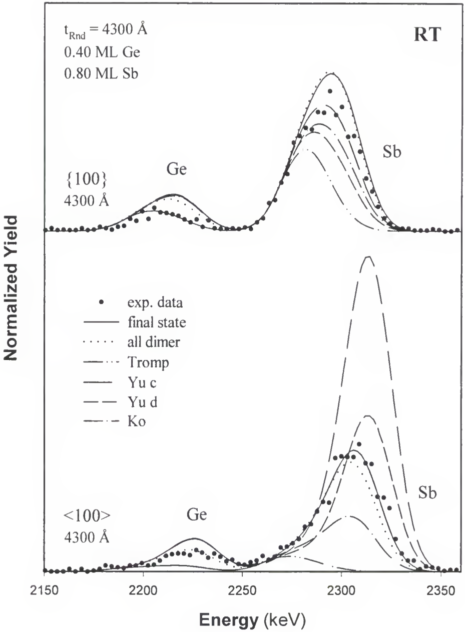

Figure 5-13. Axial and planar energy distributions for intermediate Ge coverage after room temperature deposition.

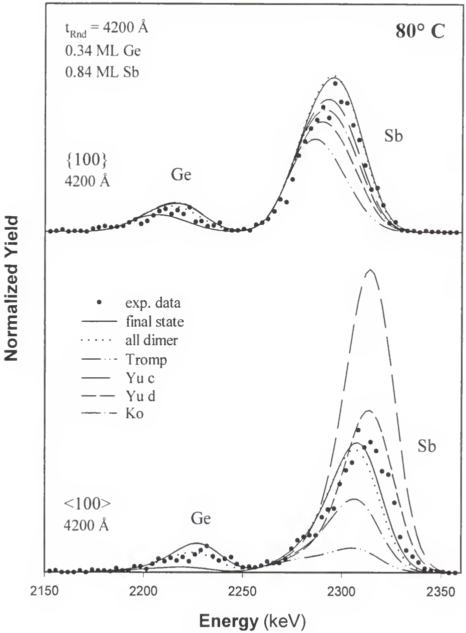

Figure 5-14. Axial and planar energy distributions for intermediate Ge coverage after annealing at 80° C.

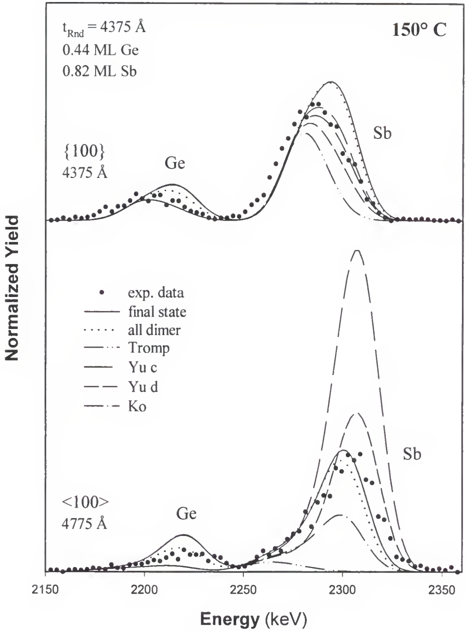

Figure 5-15. Axial and planar energy distributions for intermediate Ge coverage after annealing at 150° C.

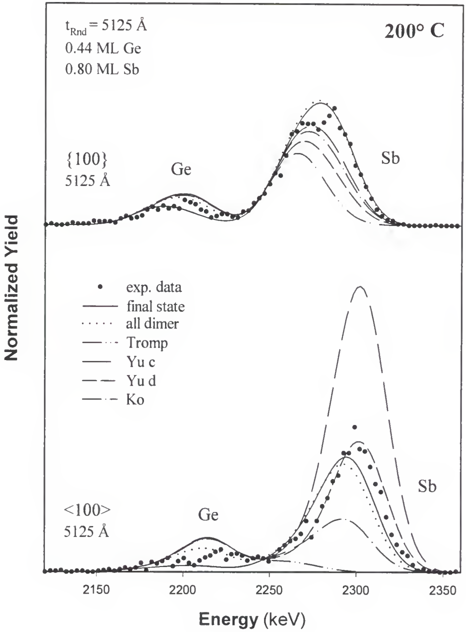

Figure 5-16. Axial and planar energy distributions for intermediate Ge coverage after annealing at 200° C.

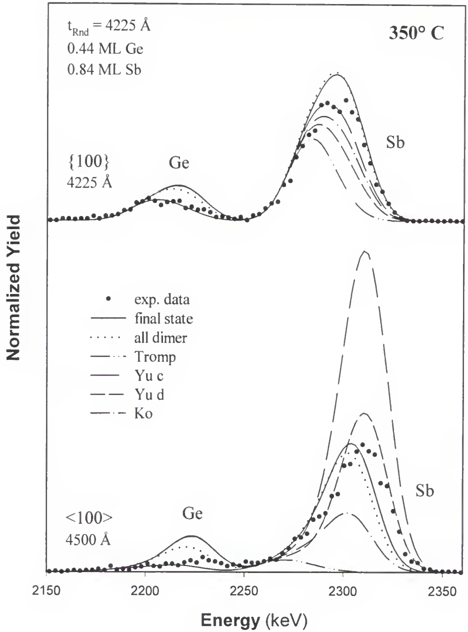

Figure 5-17. Axial and planar energy distributions for intermediate Ge coverage after annealing at 350° C.

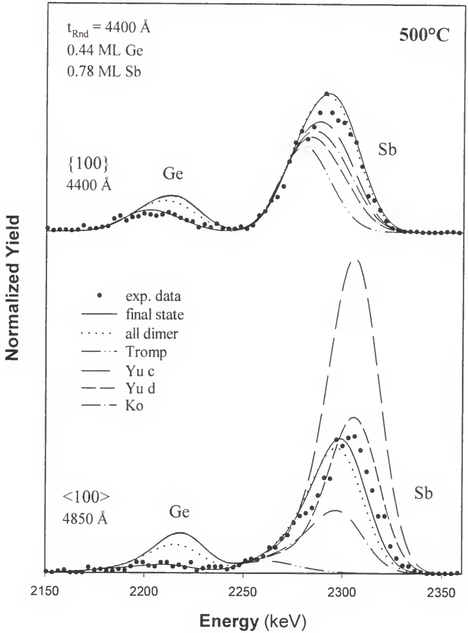

Figure 5-18. Axial and planar energy distributions for intermediate Ge coverage after annealing at 500° C.

(Figure 5-17) and 500° C (Figure 5-18) axial and planar distributions, the experimental data have reached a good fit to the final state simulation, especially for the 500° C case. Another noteworthy observation is that the half order spots in the LEED pattern for the 500° C sample disappeared after RT Ge deposition and reappeared after the anneal at 500° C. Previously we had thought that the system would reach the final state upon annealing at 350° C, but the better fit and the LEED pattern change indicate that perhaps the transition is not complete until annealing at 500° C.

An examination of the Sb peaks in the axial distributions reveals that we can reject the Tromp, Yu c, and Ko models at all of the temperatures investigated. Based only on the comparison of experimental to simulated yield, as represented by peak height, none of these configurations fits the data. The Yu c configuration is too high because half of the Sb is in near-interstitial dimer sites, and the Tromp and Ko models fall well below the data because all and half, respectively, of the Sb is substitutional. The planar data are less clear, but the Tromp model still fails whereas the Yu c and Ko models cannot be eliminated from consideration based only on these data.

Shifting our focus from the yield comparisons in the Ge and Sb peaks to the position on the energy axis of the Sb data relative to the simulations, we find reason for concern. During the initial analysis of the 80° C axial energy distribution, the shift of the Sb data to higher energy relative to the final state and all dimer simulations led to optimism about our having found the interstitial Sb dimers of the Yu model. When this shift persisted through the 500° C energy distributions, however, other explanations were required.

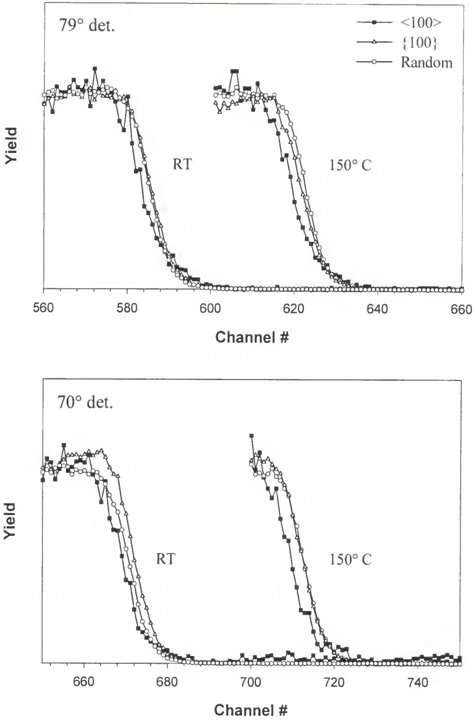

Figure 5-19. High energy edges of Si peak for RT and 150° C data. (Random and {100} spectra have been scaled for easy comparison of Si half-heights. Also, the 150° C data have been shifted to the right to separate the two sets of data.)

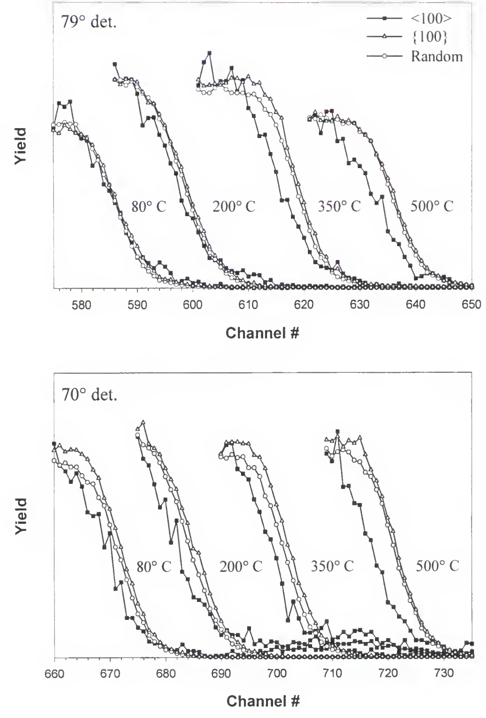

Figure 5-20. High energy edges of Si peak for 80° C, 200° C, 350° C, and 500° C data. (Random and {100} spectra have been scaled for easy comparison of Si half-heights. Also, each higher temperature data set has been shifted to the right.)

The first place to look is the shifts in the high energy edges of the Si peaks for the various spectra. Figure 5-19 shows the shifts for the RT and 150° C data, and Figure 5-20 shows the shifts for the other four sets of data. (They are shown in two separate figures because they were obtained from two different samples.) When the shift between axial and random Si peaks was two channels or more, we used Monte Carlo ion distributions obtained for the greater thickness associated with the shift, as described in Chapter 4. Based on this criterion, we used greater thicknesses for the axial data taken after the 150° C, 350° C, and 500° C anneals.

The effect of greater thickness is to shift the simulations to lower energy relative to the data. Although not shown, the simulated energy distributions for the final state and all dimer model fit the Sb data well before adjusting the thickness for the three cases mentioned above. We cannot justify omitting the thickness adjustment, however, because, as was shown in Chapter 4, the axial Ge and Sb peaks move to lower energy when the axial Si peak shows a shift relative to the random Si peak. We also showed in Figure 4-13 that a sample with a large amount of thickness variation gives rise to a large spread in the high energy edges of the Si peaks, whereas a sample with little thickness variation produces Si peaks that overlap well (Figure 4-12).

In the analyses of our 0.15 ML, 0.68 ML, and 2 ML data, this change in thickness resulted in simulations that fit the data well, the determining factor being the energy distributions obtained at 350° C or 500° C. At these temperatures, we know from previous experiments [Gra94b, Bos96c] that the system is best described by the atomic configuration we call the final state, which was determined from these experiments.

Based on our experience with this system, we feel certain that the Sb and Ge are in the final state. Thus the discrepancy between data and simulations must have another cause.

To this point we have shown that thickness variation can be seen by the interference fringes in the thin window, that thickness variation results in the Si peaks not overlapping on the high energy edge, that the Ge and Sb peaks also shift when the Si peak does, and that adjusting for thickness variation does not always solve the problem with fitting the energy distributions. One possible explanation is spontaneous gain shifts in the electronics. We had these problems earlier and fixed them, and also the consistency of the shift in both the 79° and 70° detectors argues against electronic causes.

A trend evident in Figure 5-20 hints at the energy shift between the axial and random spectra being induced by annealing, as the shift grows with increasing temperature. Figure 4-14 indicates otherwise, however. In that figure, the only difference between the two sets of data (one showing a large shift and the other showing none) is that they were obtained from two different spots on the same sample. They had the same Ge and Sb coverages, both were obtained after RT Ge deposition, and the detector bias voltage had not been turned off between data sets. The trend in Figure 5-20, therefore, does not necessarily imply any causal relationship between energy shift and temperature of anneal.

A trend in the Si peak shifts that is consistent is the <100> Si peak being shifted to lower energy relative to the random and {100} spectra. If the shifts were attributable only to thickness variation, then the random should be shifted to lower energy as often as the axial, and the planar spectrum should show the same behavior. The shifts in our data suggest that the ion beam experiences greater energy loss than expected in the axial direction because of some other mechanism.

Schell-Sorokin and Tromp, in a study of the strain in epitaxial Ge on Si(100), have proffered one possible mechanism [Sch90]. They measured the radius of curvature for a 100 μm thick Si crystal that bent during the epitaxial growth of Ge on the surface. The deformation, they said, was due to the strain of the Ge layer and was significant even at submonolayer Ge coverage. It is reasonable to expect that if they found bending in a 100 μm thick Si crystal, then our thin windows, which are 0.5 μm thick and supported by 500 μm of Si, would be subject to deformation. The constraint of having the thin window surrounded by thicker Si, however, complicates visualization of how the deformation would occur.

To check for a correlation between Ge and the energy shifts, we collected scattering data from a thin window that had no Ge. The high energy edges of the Si peaks for a Si(100) sample with the Shiraki oxide intact are shown in Figure 5-21. For the clean Si(100)-2x1 surface, the high energy edges of the Si peaks are shown for the beam incident on the center spot in Figure 5-22 and on an outer spot in Figure 5-23.

In Figure 5-21, the first three sets of Si peaks contain the same <100> data compared with three different random spectra, and the last set compares the axial data from the first three sets with a second axial spectrum taken at the end of the experiment. The bulge noticeable at the high energy side of the Si in the axial spectra is the result of scattering from Cl, a remnant of the Shiraki oxidation procedure [Ish86]. Ignoring that peak, the axial and random spectra appear to overlap well. The three random spectra were obtained on different sides of the <100> axis to check for thickness variation as we tilted

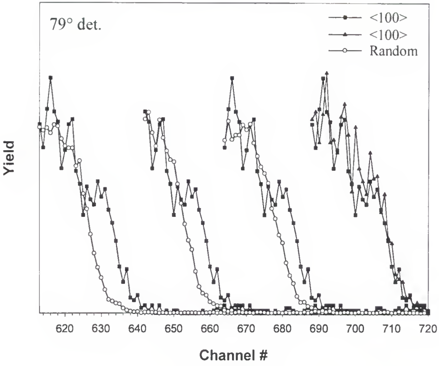

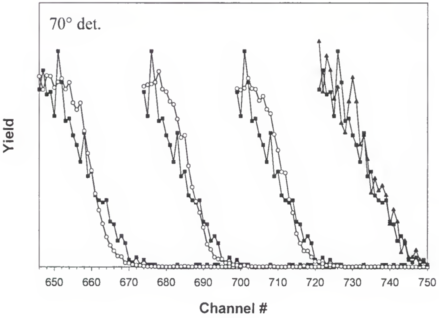

Figure 5-21. High energy edges of Si peak for Si(100) with Shiraki oxide intact. (Random spectra have been scaled for easy comparison of Si half-heights. Also, each successive pair of spectra has been shifted to the right to separate the four sets of data.)

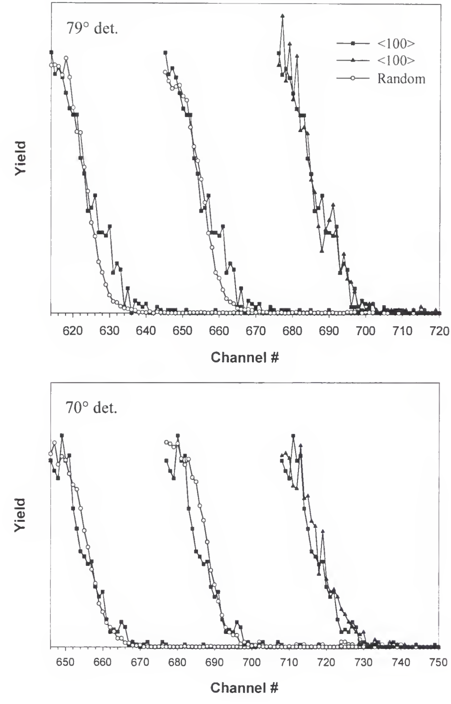

Figure 5-22. High energy edges of Si peak for the center spot on clean Si(100)-2x1. (Random spectra have been scaled for easy comparison of Si half-heights. Also, each successive pair of spectra has been shifted to the right to separate the four sets of data.)

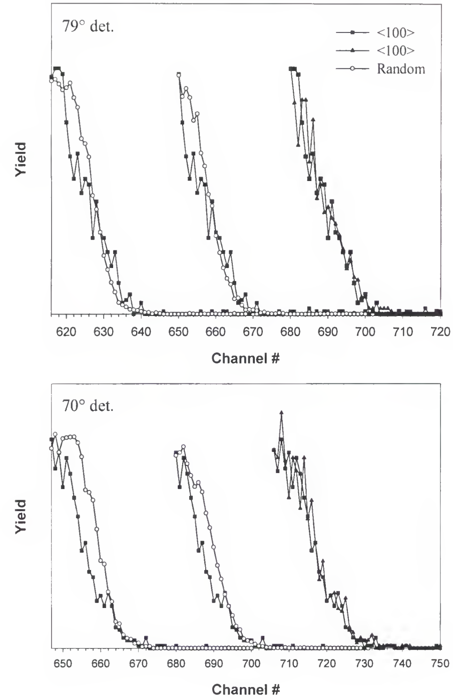

Figure 5-23. High energy edges of Si peak for an outer spot on clean Si(100)-2x1. (Random spectra have been scaled for easy comparison of Si half-heights. Also, each successive pair of spectra has been shifted to the right to separate the three sets of data.)

the sample. The second axial spectrum was obtained for the same reason, and because we had some concern that perhaps the goniometer played a role in the shifts. Based on these data, the goniometer appears to work well.

Figure 5-22 compares one axial with two different random spectra in the first two data sets and then two axial spectra in the third. These data were obtained on the center spot and show little evidence of energy shifts or thickness variation. The data from the outer spot (Figure 5-23) hint at an energy shift, especially in the 70° detector. Overall, these data for the Si(100) sample without Ge seem to indicate that the Ge may play a role in the energy shifts, although the evidence is not overwhelming.

At this point, we reached a stalemate in our attempts at understanding these energy shifts. Accordingly, we failed to learn how we might make the proper corrections for them in order to make full use of the information in our scattered ion energy distributions. Our conclusions based on the yield information are still valid, but we cannot distinguish between the final state, all dimer, and Yu d configurations when examining the Sb data.

Summary

The open questions of surfactant-mediated epitaxy, especially those dealing with the segregation of the surfactant, have led us to perform transmission ion channeling experiments for determination of the surface structure of Ge/Sb/Si(100). The work described in this chapter is in three parts: (i) testing a new exchange model with previous data, (ii) studying the Ge/Sb/Si(100) system with 2 ML of Ge deposited at room temperature and then annealed at 500° C, and (iii) investigating the surface structure with

0.4 ML Ge on Sb/Si(100) after RT Ge deposition and after annealing at temperatures from 80° C to 500° C.

In the first part, we have found that the Ko model does not fit our data for this system at Ge coverages of 0.15 ML or 0.68 ML either before or after annealing the sample at 350° C. In the second part, we found that even at the high Ge coverage of 2 ML, the Ge is in the elongated dimer sites of the all dimer model. In the third part, we have found that for a Ge coverage of 0.4 ML, the Ge goes from the all dimer model to the final state, passing through an intermediate state at intermediate temperatures. Although the Sb does not fit the Tromp, Yu c, or Ko models, we cannot distinguish between the all dimer, final state, and Yu d configurations because of anomalous energy loss that appears intermittently in the axial energy distributions. Thickness variation can cause the type of energy shifts we see, but some other mechanism also appears to be involved. One candidate is deformation of the thin window because of strain in the Ge layer.

CHAPTER 6
DIMER ELONGATION ON THE MONOHYDRIDE-COVERED GE/SI(100) SURFACE

Background

The H/Ge/Si(100) system is similar to Ge/Sb/Si(100) in that both Sb and H can act as surfactants and change the growth mode of Ge on Si(100) from Stranski-Krastanov (layer by layer followed by islanding) to Frank-Van der Merwe (layer by layer) [Cop90, Cop91, Sak94]. The mechanism responsible for the change differs in the two cases, but the result is the same: smooth Ge layers on Si(100). Instead of investigating the details of the change in growth mode, however, in this case we have studied the structural changes induced in epitaxial Ge on Si(100) by the adsorption of H [Bai98b]. In that regard, we will briefly review what is known about H adsorption on Si(100), on Ge(100), and on Ge/Si(100), as well as the epitaxial growth of Ge on Si(100). (See Chapter 5 for details about the clean Si(100)-2x1 surface.)

The discovery of the 1x1 phase upon H adsorption onto the clean Si(100)-2x1 surface [Saku76] ignited a tremendous effort to understand the H/Si(100) surface structure [Zhe92, Cra90, Lu92, Qin96, Sho93, Bol90, Bol92, Cha85, Wan93a, Wan93b, Wam95]. The initial conception had the 2x1 monohydride surface (one H atom occupying the dangling bond on each Si dimer atom) evolving into a well-ordered 1x1 dihydride surface (two H atoms per Si atom, Si dimers broken, and Si atoms in bulk-like sites) at saturation H coverage of 2 monolayers (ML) [Saku76]. Discovery of the 3x1 phase (alternating monohydride and dihydride) led to the suggestion that the 1x1 phase was merely disordered regions of the 3x1 phase and that the saturation H coverage was less than 2 ML [Cha85]. Scanning tunneling microscopy (STM) studies [Bol90, Bol92] indicated that the 1x1 phase is actually a disordered dihydride layer. Furthermore, etching of the Si back bonds has been observed in the 1x1 phase [Lu92, Bol90, Bol92].

Because Ge(100) reconstructs in the same way as Si(100), the surface geometry of H/Ge(100) also has been studied [App78, Cha86, Cul86, Pap86, Cho92]. Early efforts [App78, Cha86, Cul86] failed to produce the 1x1 phase on this surface, perhaps because of sample temperature or inadequate H exposure. This phase has since been produced [Pap86, Cho92] but may be due to a disordered monohydride rather than a dihydride surface[Cho92]. That the Ge-H bonds are ~15% weaker than Si-H bonds [Ham90] could make the dihydride surface on Ge(100) unstable [Cho92].

The epitaxial growth of Ge on Si(100) is another technologically important field, and much work has been done to understand the morphology and growth patterns of this system. For submonolayer Ge adsorption, which is the regime addressed in this work, the dimer bond geometry has been measured and calculated in several ways [Gra94c, Fon93, Oya95, Kru94, Jin94, Jen97a]. The Ge dimer bond length varies from 2.51 Å to 2.60 Å when measured experimentally [Gra94c, Fon93, Oya95] and from 2.34 Å to 2.48 Å when determined theoretically [Kru94, Jin94, Jen97a]. In all of these cases except one, the Ge dimers were found to be tilted from 12° to 19°. The one exception reported symmetric, unbuckled Ge dimers [Oya95]. For the scarcely studied case of H adsorbed onto submonolayer Ge on Si(100), researchers have looked at the desorption of H from the surface [Boi96] and have studied the surfactant effect of H [Cop91, Sak94, Kah97].

In this work, we report the first measurement of the Ge dimer bond geometry for the H/Ge/Si(100)-2x1 system. Following preparation of the 1 ML H on 0.9 ML Ge on Si(100)-2x1 surface, we measured the Ge adatom positions using transmission ion channeling and found a significant difference from the result for Ge/Si(100) without H. The dimer bond in the H-covered case is elongated and shows no buckling. This change is consistent with what has been found for Si dimers on the Si(100) surface with and without H [Zhe92, Cra90, Wan93a]. Although one of our goals in this research was to determine the H geometry, problems with distinguishing between H on the front and back surfaces of the sample and with H desorption during ion bombardment made this goal unattainable.

Experiment

The Ge adatom positions were determined by transmission ion channeling, but, rather than fitting energy distributions as in chapter 5, we used angular scans (yield versus tilt angle) in this case. (See chapter 4 for details.) Briefly, this method takes advantage of the non-uniform ion flux as a channeled ion beam emerges from a thin crystal. Because of this non-uniform flux, which peaks in the middle of each channel, the scattering yield from an adatom on the beam exit side of the crystal depends on the adatom's position in the channel. By comparing experimental angular scans (scattering yield versus tilt angle) with calculated angular scans, we can determine the adatom positions with a typical resolution of 0.1 Å. We have used the continuum approximation with a 25 string Doyle Turner potential to calculate angular scans for different adatom positions [Bec88a, Bec88b].

Samples were prepared *ex situ* as described in chapter 2 and then placed in the UHV preparation chamber (base pressure ~5×10^{-11} Torr). After the sample was degassed thoroughly, the oxide was desorbed with a heat lamp. At this point, LEED yielded a two-domain 2x1 pattern with low background and sharp spots, indicating a properly prepared Si(100) surface. With the sample heated to 350° C, Ge was deposited from an effusion cell at the rate of 0.15 ML/min. The LEED pattern remained the same (2x1) except for slightly higher background. With the sample at room temperature, H was deposited by passing H_2 over a tungsten filament in a tube aimed at the sample. The total H exposure was 5000 Langmuirs (5×10^{-6} Torr for 10^3 s), resulting in a 1x1 LEED pattern that indicated coverage of the surface with a dihydride layer. The return of the two domain 2x1 LEED pattern upon annealing the sample to 300° C indicated that we had recovered the monohydride surface. The Ge coverage, determined by Rutherford backscattering, was 0.9 ML, and the H coverage, determined by elastic recoil detection analysis, was 1.8 ML. The measured H coverage included contributions from both sides of the sample, and thus was near 1 ML on the Ge-covered surface.

With sample preparation complete, the sample was transferred under vacuum to the scattering chamber (base pressure 5×10^{-11} Torr) and placed on a two-axis goniometer. A differentially pumped beamline connects the scattering chamber to a 3.5 MV Van de Graaff accelerator. The 2.5 MeV He^+ beam enters the chamber with an angular divergence of 0.03° and is confined by slits to a 1x1 mm^2 area on the sample. By observing the pattern produced by the beam on a piece of quartz at the end of the beam line, we found the channeling directions used in the experiment. The accuracy of alignment was measured to be approximately 0.05°.

The tilt angles, θ, used in the angular scans start at the axial channeling direction (0.0°) and gradually increase to 6.0° for the <100> scan and 5.0° for the <110> scan. To avoid planar channeling effects as the sample is tilted away from the axis, we used the methodology of Ref. [Dyg93] to identify the lab coordinates necessary to tilt outward at an azimuthal angle, φ, of 15° from the {110} plane for the <100> scan and 10° from the {100} plane for the <110> scan. These directions were found by computer simulation to be relatively free of planar influences, with the final points at (θ, φ) = (6.0°, 15°) and (5.0°, 10°) being good approximations to "random" directions [Dyg94a, Dyg94b, Dyg94c]. Three passivated, ion-implanted solid state detectors collected and energy analyzed scattered ions at scattering angles of 79° and 150° and H recoils at an 18° scattering angle. The integrated beam current of each spectrum was limited to 24 μC (1.5×10^{16} ions cm^{-2}) to minimize damage to the Si crystal. Figure 6-1 shows the spectra for <100> and random beam incidences as well as the scattering geometry for the 79° detector, which was used to collect the Ge angular scan data.

Results and Discussion

Ge Dimer Geometry

The experimental data and calculated angular scans are shown in Figure 6-2. The open and closed circles show the experimental Si and Ge yields, respectively, with error bars shown for the Ge data. Each data point is normalized by dividing the yield by the corresponding (Si or Ge) random yield. The dashed curves represent the angular scans calculated for a substitutional site; the solid curves are our best-fit angular scans

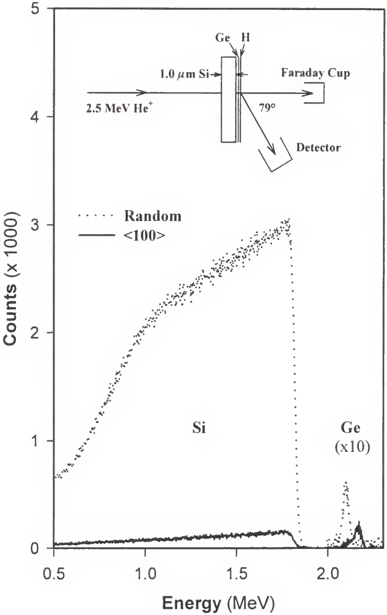

Figure 6-1. Scattering geometry and sample spectra for Ge data.

calculated for the Ge in this experiment; and the dotted curves, shown for comparison, are the calculated scans for the asymmetric Ge dimers on Si(100) (no H) found by Grant *et al.* [Gra94c].

The process for finding the best fits between the experimental and calculated Ge scans entailed independently varying the x and z positions of two Ge atoms and finding the minimum χ^2 values. (The x direction is along the (110) plane, and the z value gives the height relative to the (001) surface plane.) Using two atoms allowed for the possibility of asymmetric dimer sites. We did not consider "twisted" dimers, in which the atoms move out of the (110) plane (i.e., no y iterations). Since the <100> scan provides information only about the lateral positions of the adatoms and not their height above the substrate, we found the optimal values for x from this scan. We then used the <110> scan to determine the z values. One other parameter that we investigated was the Ge vibrational amplitude. We found, as did Grant [Gra94c], that large and anisotropic vibrations yielded slightly better fits but that the system was over-parametrized and the only difference in the resulting site was a shift along x of 0.16 Å. Therefore, we used the two-dimensional vibrational amplitude of 0.14 Å that Grant [Gra94c] used and that is based on calculations by Alerhand, Joannopoulos, and Mele [Ale89].

The result of this fitting process shows that the Ge dimers are elongated, shifted along x, and not buckled. We found a dimer bond length of 2.8±0.1 Å, a shift off-center of 0.16±0.05 Å along x, and a height of 0.0±0.2 Å relative to the top layer bulk lattice sites (i.e., no relaxation). With the exception of the 0. 3° to 0. 6° range in the <110> scan,

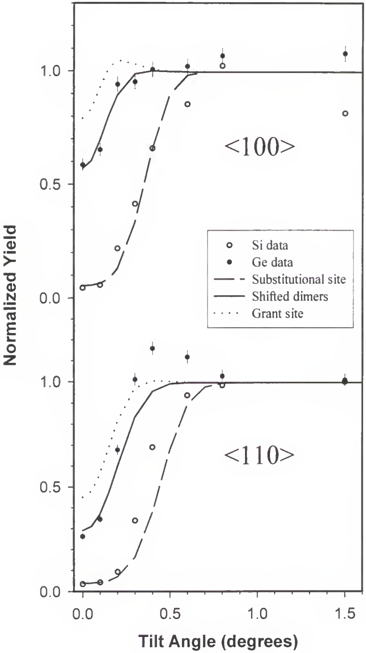

Figure 6-2. Ge angular scans.

our calculated angular scans describe the Ge data well. The data points at tilts of 0.3°, 0.4°, and 0.6° reside above the calculated scans for both Ge and Si. The most likely explanation of this discrepancy is an error of 0.1° in finding the <110> channeling direction (whereas we typically find channeling directions to within 0.05°) and an inability of the continuum model to fit "shoulders" in angular scans. It can also be seen that calculated scans for the asymmetric dimer sites found by Grant [Gra94c] for Ge/Si(100) without H clearly do not fit our data. Figure 6-3 shows the geometry of the site that we found for H/Ge/Si(100) and the site found by Grant [Gra94c] for Ge/Si(100). The dimer bond length of 2.8 Å that we found is 8% larger than the 2.6 Å found by Grant [Gra94c], a change that is consistent with the dimer elongation found for Si with and without H coverage (Table 6-1).

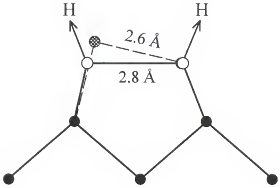

Figure 6-3. Ge dimer geometry. Solid circles represent Si atoms, open circles are the Ge sites found in this work, and cross-hatched circles show the sites found by Grant *et al.* [Gra94c].

Three potential complicating factors need to be discussed: (i) etching of the back bonds by H, (ii) Ge-Si interdiffusion, and (iii) coverage dependence of the Ge positions.

Table 6-1. Dimer Elongation upon H Adsorption

	DBL w/o H*	*DBL* w/ H*	*% change*	*reference*
Si(100)	2.13 Å	2.37 Å	11	Zhe92
Si(100)	2.14 Å	2.37 Å	11	Cra90
Si(100)	2.26 Å	2.97 Å	31	Wan93a
Ge/Si(100)	2.6 Å	2.8 Å	8	Gra94c, Bai98b

* DBL = dimer bond length

Etching is thought to occur on the H/Si(100)-1x1 surface due to the strain in the back bonds of dihydride units [Bol92]. Since the H/Ge(100)-1x1 surface may be due to disordered monohydrides [Cho92]—a dihydride on Ge having been observed only once [Pap86]—etching may not occur in this case. Also, Eaglesham, Unterwald, and Jacobsen, who looked at the effects of annealing Ge/Si(100) in a flux of H, found no significant etching of Ge [Eag93]. The 2x1 LEED pattern and H coverage of ~1 ML after annealing at 300° C suggest that we have obtained an ordered monohydride on Ge/Si(100).

The second complicating factor, observed in experiment and calculations [Jen97a, Pat95], is the diffusion of Ge into the Si substrate. This interdiffusion would lead to a portion of the Ge being in bulk-like sites and would cause our angular scans to dip lower in the channeling directions. To fit the data by including some Ge in bulk-like sites would require the dimer bonds to be shorter. We are primarily interested in how our result compares to Grant's [Gra94c], since his result derives from the same technique—and even the same equipment—and thus would have been subject to the same problem.

The third problem is perhaps the most serious. Grant found a trend toward deeper and broader dips in the angular scans near the <111> direction as the Ge coverage increased from 0.26 ML to 0.90 ML [Gra94c]. Also, Knall and Pethica [Kna92] found a small amount of second layer growth as the Ge coverage increased toward 1 ML. Both of these points would indicate that perhaps our fitting procedure should include a mix of bulk-like and dimer sites. We tried this and found that for Ge dimers in the Grant sites, ~30% of bulk-like Ge is necessary to reproduce the measured yield for the tilt of 0.0° for H/Ge/Si(100). The rest of the points in the scan, however, fit poorly. Therefore, although there may be a small component of the Ge in bulk-like sites, its effect on our conclusion of elongated dimers appears to be minimal. Further, Grant's <100> angular scans at the coverages mentioned above do not show a trend toward coverage-dependent sites [Gra94a].

Hydrogen Recoil Data

In addition to investigating the Ge structure for H/Ge/Si(100), we also had as a goal the determination of the H sites. To that end, we used a detector placed at a scattering angle of 18° to detect H recoils so that we could analyze angular scans for the H data. Figure 6-4 shows the scattering geometry for detecting recoiled H atoms and a typical H spectrum. The small mass of H limits the resolution with which we could find the H sites because it enhances the two-dimensional vibrational amplitude, ρ_{2D}. Wampler, in his transmission ion channeling study of D/Si(100), found that he had to use $\rho_{2D} = 0.4$ Å to obtain good fits to his data [Wam95].

Further problems, however, prevented the poor resolution from becoming an issue. The H spectrum shown in Figure 6-4 contains contributions from H scattered from both sides of the thin sample, and the small number of counts in the peaks makes an accurate deconvolution impossible. Since we cannot separate the front and back side

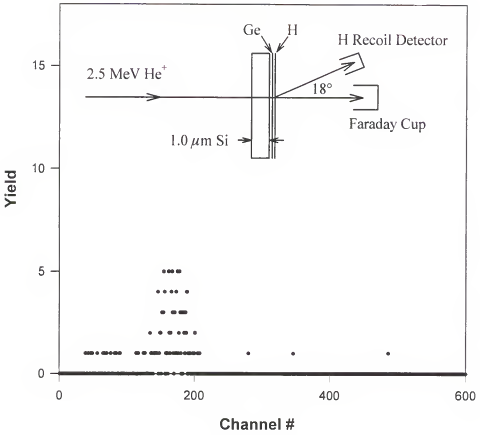

Figure 6-4. Hydrogen recoil spectrum and scattering geometry.

contributions, we also cannot analyze the angular scans. The structural information is carried by the H recoils from the beam-exit side of the sample because the H atoms on that side interact with the channeled He$^+$ beam and its nonuniform flux distribution. Another problem with the H data was the desorption of H from the surface during the experiment. To test for desorption, we took ten spectra in the random direction and then ten spectra in the <100> direction, each for a dose of 10 μC, and monitored the H yield. The data are shown in Figure 6-5 and clearly show a loss of H during irradiation, especially in the <100> direction. The result of these problems is that we can say nothing about the H sites in this experiment.

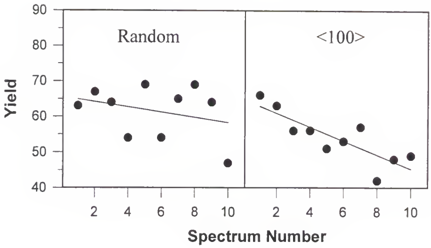

Figure 6-5. Consecutive spectra in random and <100> directions showing evidence of H desorption. (The line in each graph is a linear regression.)

Summary

Using transmission ion channeling, we have found that a monolayer of H on the Ge/Si(100)-2x1 surface causes elongation of the Ge dimers from 2.6 Å, as found by Grant *et al.* [Gra94c], to 2.8 Å and that the dimers are shifted by 0.16 Å along the {110} plane and are no longer buckled. (A tilt of up to 8° cannot be ruled out however.) This change in the dimer bond length is similar to that reported for dimers on the Si(100) surface before and after adsorption of a monolayer of H. Although etching of the Si back bonds by H has been observed for H/Si(100)-1x1, we believe that it may not be a problem for H/Ge/Si(100). Also, Ge-Si interdiffusion and Ge coverage-dependence of sites may cause our result to be skewed to a slightly longer dimer bond length than exists on the surface. In the former case, the result of Grant *et al.* [Gra94c] should be subject to the same problem, and in the latter, we have found that coverage-dependence has a minimal effect on our result. Finally, because of problems with separating the front and back side contributions to the H recoil spectra and with H desorption, we can say nothing about the geometry of the H atoms on this surface.

CHAPTER 7
CONCLUSION

The work presented in this dissertation concerns the epitaxial growth of Ge on Si(100), an area of great technological interest. We have sought to understand details of the surface structure under varying growth conditions for two separate systems. We first studied surfactant-mediated epitaxy (SME) in the Ge/Sb/Si(100) system before and after annealing. The method of analysis used for this study was comparison of experimental energy distributions with simulated energy distributions based on a Monte Carlo simulation of the channeling process. Although we found this method of analysis to have some drawbacks that hampered our ability to distinguish between several possible states of the system, we were able to rule out certain theoretical models from the literature. The second system we studied was H/Ge/Si(100). We prepared the monohydride-covered Ge/Si(100) surface and determined the Ge adatom positions on the surface.

In studying the Ge/Sb/Si(100) system, we had hoped to gain enough information about the surface structure at different temperatures that we could make a clear determination of the mechanism involved in the adatom-surfactant exchange process as the surfactant segregates to the top layer during growth. The first part of this study was to compare simulated energy distributions for a new exchange model (the single adatom exchange model) with the experimental energy distributions that we had compared with two previous models. Based on the peak heights in the distributions, we found this new model not to be described by our previously obtained data for Ge coverages of 0.15 ML and 0.68 ML. The axial distributions fit the data neither before nor after annealing the sample at 350° C.

The second part of this study was basically the same experiment as just described except with a higher Ge coverage (2 ML). Somewhat surprisingly, we found the system after room temperature Ge deposition to be in the same state that we had found for the 0.68 ML coverage mentioned above. That is, the Ge was in dimer-like sites with a dimer bond length of 2.8 Å, whereas Ge on Si(100) dimers have a bond length of 2.6 Å [Gra94c]. The Sb also was found in dimer sites that appear to be similar to those described by the experimentally-determined final state configuration [Gra94b, Bos96c]. Upon annealing the sample at 500° C, the Ge moved to near-substitutional sites, and the Sb appears to be in dimer sites with a greater amount of disorder.

In the third part of this study, we deposited 0.4 ML of Ge at room temperature and annealed the sample incrementally from 80° C to 500° C, collecting scattered ion energy distributions after each stage. This is the set of experiments that we hoped would lead to determination of the exchange mechanism in SME.

After obtaining many data, our efforts at understanding the system were impeded by issues involved in the method of analysis. First, we found planar oscillations in the {110} direction. These oscillations occur with a wavelength of 600-700 Å, which is small enough that our thickness resolution of ~100 Å can make a large difference in the appearance of a simulated energy distribution. Second, we found evidence for thickness variation in the samples that could effect the position of energy distributions on the energy axis. Finally, we concluded that thickness variation was not enough to explain the energy shifts we saw in our energy distributions and that strain in the Ge layer may cause deformation of the crystal, thereby increasing the ion energy loss in the axial direction.

Based on the yield information, however, we can say that the Ge starts out in the elongated dimer sites of the all dimer model, passes through an intermediate state in the 150° C to 200° C range, and then reaches near-substitutional sites of the final state at 350° C to 500° C. Although the energy shifts mentioned previously prevent us from distinguishing between Sb in the final state, all dimer, or Yu d models, we can safely eliminate the Tromp and Ko models, which both have substitutional Sb, and the Yu c configuration, which has a high proportion of interstitial Sb dimers.

In the other system that we studied, H/Ge/Si(100), we used the angular scan (yield versus tilt) method of analysis to determine the Ge positions. With 0.9 ML of Ge and ~1 ML of H on the surface, we found the Ge to be in dimer sites that showed significant differences from the dimers of Ge on Si(100) without H. These dimers have a bond length of 2.8 Å, are shifted 0.16 Å off center, and are not buckled. In contrast, the dimers for this system without H are 2.6 Å long, are shifted 0.07 Å off center, and have a tilt of 12°.

Finally, we have added to the store of knowledge about the structure of Ge in the presence of Sb and of H on the Si(100) surface. Because of limitations that we discovered with the method of analyzing energy distributions, we were not able to make a final determination of the exchange mechanism in surfactant-mediated epitaxy. We did find an interesting result, however, for the system at room temperature with a high Ge coverage. We also monitored the change in Ge sites from dimer to intermediate to substitutional as the annealing temperature increased to 500° C and ruled out two of the three models proposed in the literature.

REFERENCES

Abe75 F. Abel, G. Amsel, M. Bruneaux, C. Cohen, and A. L'Hoir, *Phys. Rev.* B **12**, 4617 (1975).

Ale89 O. L. Alerhand, J. D. Joannopoulos, and E. J. Mele, *Phys. Rev.* B **33**, 12622 (1989).

App78 J. A. Appelbaum, G. A. Baraff, D. R. Hamann, H. D. Hagstrum, and T. Sakurai, *Surf. Sci.* **70**, 654 (1978).

Asa85 M. Asai, H. Ueba, and C. Tatsuyama, *J. Appl. Phys.* **58**, 2577 (1985).

Bai98a A.A. Bailes III, M.A. Boshart, and L.E. Seiberling, *Nucl. Instrum. Methods* B **136-138**, 804 (1998).

Bai98b A.A. Bailes III, M.A. Boshart, and L.E. Seiberling, *Surf. Sci. Lett.* **410**, L762 (1998).

Bar86 S. A. Barnett, H. F. Winters, and J. E. Greene, *Surf. Sci.* **165**, 303 (1986).

Barr71 J. H. Barrett, *Phys. Rev.* **3**, 1527 (1971).

Barr76 J. H. Barrett, F. Fujimoto, K. Komaki and Y. Hashimoto, *Radiat. Eff.* **28**, 119 (1976).

Bec88a B. Bech Nielsen, *Phys. Rev.* B **37**, 6353 (1988).

Bec88b B. Bech Nielsen , Ph.D. Dissertation, University of Aarhus (1988).

Bev86 J. Bevk, J. P. Mannaerts, L. C. Feldman, B. A. Davidson, and A. Ourmazd, *Appl. Phys. Lett.*, **49**, 286 (1986).

Boi96 G. Boishin and L. Surnev, *Surf. Sci.* **345**, 64 (1996).

Bol92 J. J. Boland, *Surf. Sci.* **261**, 17 (1992).

Bol90 J. J. Boland, *Phys. Rev. Lett.* **65**, 3325 (1990).

Bos95a M.A. Boshart, A.A. Bailes III, A. Dygo, and L.E. Seiberling, *J. Vac. Sci. Technol.* A **13**, 2764 (1995).

Bos95b M.A. Boshart, A. Dygo, and L.E. Seiberling, *Phys. Rev.* A **51**, 2637 (1995).

Bos96a M.A. Boshart, Ph.D. Dissertation, University of Florida (1996).

Bos96b M.A. Boshart, A.A. Bailes III, and L.E. Seiberling, *Phys. Rev. Lett.*, **77**, 1087 (1996).

Bos96c M.A. Boshart, A.A. Bailes III, and L.E. Seiberling, *Surf. Sci. Lett.* **348**, L75 (1996).

Bre96 M. B. H. Breese, P. J. C. King, G. W. Grime, P. J. M. Smulders, L. E. Seiberling, and M. A. Boshart, *Phys. Rev.* B **53**, 8267 (1996).

Cao92 R. Cao, X. Yang, J. Terry, and P. Pianetta, *Appl. Phys. Lett.* **61**, 2347 (1992).

Cha85 Y. J. Chabal and K. Raghavachari, *Phys. Rev. Lett.* **54**, 1055 (1985).

Cha86 Y. J. Chabal, *Surf. Sci.* **168**, 594 (1986).

Che80 N. W. Cheung, Rev. Sci. Instrum. **51**, 1212 (1980).

Che81 N. W. Cheung and J. W. Mayer, *Phys. Rev. Lett.* **46**, 671 (1981).

Cho92 J. Cho and R. J. Nemanich, *Phys. Rev.* B **46**, 12421 (1992).

Chu78 W. K. Chu, J. W. Mayer, and M. A. Nicolet, *Backscattering Spectrometry* (Academic Press, New York, NY, 1978).

Cop89 M. Copel, M.C. Reuter, E. Kaxiras, and R.M. Tromp, *Phys. Rev. Lett.* **63**, 632 (1989).

Cop90 M. Copel, M.C. Reuter, M. Horn von Hoegen, and R.M. Tromp, *Phys. Rev.* B **42**, 11682 (1990).

Cop91 M. Copel and R. M. Tromp, *Appl. Phys. Lett.* **58**, 2648 (1991).

Cra90 B. I. Craig and P. V. Smith, *Surf. Sci. Lett.* **226**, L55 (1990).

Cul86 R. J. Culbertson, Y. Kuk, and L. C. Feldman, *Surf. Sci.* **167**, 127 (1986).

Dab92 J. Dabrowski and M. Scheffler, Appl. *Surf. Sci.* **56-58**, 15 (1992).

Dav27 C. J. Davisson and L. H. Germer, *Phys. Rev.* **30**, 705 (1927).

Dep98 P. De Padova, R. Larciprete, C. Quaresima, C. Ottaviani, C. Comicioli, C. Crotti, M. C. Håkansson, M. Peloi, B. Ressel, and P. Perfetti, *Appl. Surf. Sci.* **123-124**, 641 (1998).

Doy68 P. A. Doyle and P. S. Turner, *Acta. Cryst.* A **24**, 390 (1968).

Dyg88 A. Dygo and A. Turos, *Phys. Lett.* A **127**, 281 (1988).

Dyg89 A. Dygo and A. Turos, *Phys. Rev.* B **40**, 7704 (1989).

Dyg92 A. Dygo, P. J. M. Smulders, and D. O. Boerma, *Nucl. Instrum. Methods* B **64**, 701 (1992).

Dyg93 A. Dygo, W. N. Lennard, and I. V. Mitchell, *Nucl. Instrum. Methods* B **74**, 581 (1993).

Dyg94a A. Dygo, M. A. Boshart, L. E. Seiberling, and N. M. Kabachnik, *Phys. Rev.* A **50**, 4979 (1994).

Dyg94b A. Dygo, W. N. Lennard, I. V. Mitchell, and P. J. M. Smulders, *Nucl. Instrum. Methods* B **84**, 23 (1994).

Dyg94c A. Dygo, W. N. Lennard, I. V. Mitchell, and P. J. M. Smulders, *Nucl. Instrum. Methods* B **90**, 161 (1994).

Eag93 D. J. Eaglesham, F. C. Unterwald, and D. C. Jacobson, *Phys. Rev. Lett.* **70**, 966 (1993).

Fal96 J. Falta, D. Bahr, G. Materlik, B. H. Müller, and M. Horn-von Hoegen, *Appl. Phys. Lett.* **68**, 1394 (1996).

Fel82 L. C. Feldman, J. W. Mayer, and S. T. Picraux, *Materials Analysis by Ion Channeling* (Academic Press, New York, NY, 1982).

Fel86 L. C. Feldman and J. W. Mayer, *Fundamentals of Surface and Thin Film Analysis* (Elsevier, New York, NY, 1986).

Fit98 E. A. Fitzgerald and L. C. Kimerling, *MRS Bulletin* **23**, 39 (1998).

Fon93 E. Fontes, J. R. Patel, and F. Comin, *Phys. Rev. Lett.* **70**, 2790 (1993).

Gra92 M. W. Grant, P. F. Lyman, J. H. Hoogenraad, and L. E. Seiberling, *Surf. Sci. Lett.* **279**, L180 (1992).

Gra94a M. W. Grant, Ph.D. Dissertation, University of Florida (1994).

Gra94b M.W. Grant, M.A. Boshart, D.J. Dieleman, and L.E. Seiberling, *Surf. Sci. Lett.* **316**, L1088 (1994).

Gra94c M. W. Grant, D. J. Dieleman, M. A. Boshart, and L. E. Seiberling, *Phys. Rev.* B **49**, 16534 (1994).

Ham90 A. V. Hama, G. D. Kubiak, and R. H. Stulen, *Surf. Sci.* **237**, 35 (1990).

Hame86 R. J. Hamers, R. M. Tromp, and J. E. Demuth, *Phys. Rev.* B **34**, 5343 (1986).

Hib94 H. Hibino, N. Shimizu, K. Sumitomo, Y. Shinoda, T. Nishioka, and T. Ogino, *J. Vac. Sci. Technol.* A **12**, 23 (1994).

Hor94a M. Horn-von Hoegen, A. Al Falou, B. H. Müller, U. Köhler, L. Andersohn, B. Dahlheimer, and M. Henzler, *Phys. Rev.* B **49**, 2637 (1994).

Hor94b M. Horn-von Hoegen, J. Falta, M. Copel, and R. M. Tromp, *Phys. Rev.* B **50**, 10811 (1994).

Hor94c M. Horn-von Hoegen, M. Copel, J. Tsang, M. C. Reuter, and R. M. Tromp, *Appl. Phys. Lett.* **66**, 487 (1994).

Ide95 T. Ide, *Phys. Rev.* B **51**, 5397 (1995).

Isa96 A. Isaacs (ed.), *A Dictionary of Physics,* (Oxford University Press, Oxford, 1996).

Ish86 A. Ishizaka and Y. Shiraki, *J. Electrochem. Soc.* **133**, 666 (1986).

Iye89 S. S. Iyer, J. C. Tsang, M. W. Copel, P. R. Pukite, and R. M. Tromp, *Appl. Phys. Lett.* **54**, 219 (1989).

Jay93 G. Jayaram, P. Xu, and L. D. Marks, *Phys. Rev. Lett.* **71**, 3489 (1993).

Jen97a S. J. Jenkins and G. P. Srivastava, *Surf. Sci.* **377-379**, 887 (1997).

Jen97b S. J. Jenkins and G. P. Srivastava, *Surf. Sci. Lett.* **384**, L886 (1997).

Jen98 S. J. Jenkins and G. P. Srivastava, *Surf. Sci. Lett.* **398**, L308 (1998).

Jin94 J. M. Jin and L. J. Lewis, *Phys. Rev.* B **49**, 2201 (1994).

Kah97 S. J. Kahng, J. Y. Park, K. H. Booh, J. Lee, Y. Khang, and Y. Kuk, *J. Vac. Sci. Technol.* A **15**, 927 (1997).

Kan95 D. Kandel and E. Kaxiras, *Phys. Rev. Lett.* **75**, 2742 (1995).

Kax95 E. Kaxiras, *Mat. Sci. Eng. B* **30**, 175 (1995).

Kna92 J. Knall and J. B. Pethica, *Surf. Sci.* **265**, 156 (1992).

Ko96 Y.J. Ko, J.Y. Yi, S.J. Park, E.H. Lee, and K.J. Chang, *Phys. Rev. Lett.* **76**, 3160 (1996).

Koh92 U. Köhler, O. Jusko, B. Müller, M. Horn-von Hoegen, and M. Pook, *Ultramicroscopy* **42-44**, 832 (1992).

Kru94 P. Kruger and J. Pollmann, *Phys. Rev. Lett.* **72**, 1130 (1994).

Kub96 J. A. Kubby and J. J. Boland, *Surface Science Reports* **26**, 61 (1996).

Leg89 F. K. LeGoues, M. Copel, and R. M. Tromp, *Phys. Rev. Lett.* **63**, 1826 (1989).

Lin95 X. W. Lin, Z. Liliental-Weber, J. Washburn, and E. R. Weber, *Phys. Rev.* B **52**, 16581 (1995).

Lind65 J. Lindhard, *Mat. Fys. Medd. Dan. Vid. Selsk.* **34**, 1 (1965).

Lu92 Z. H. Lu, K. Griffiths, P. R. Norton, and T. K. Sham, *Phys. Rev. Lett.* **68**, 1343 (1992).

Lym91a P. F. Lyman, Ph.D. Dissertation, University of Pennsylvania (1991).

Lym91b P. F. Lyman, S. Thevuthasan, and L. E. Seiberling, *J. Cryst. Growth* **113**, 45 (1991).

Mod95 *Modular Pulse-Processing Electronics and Semiconductor Radiation Detectors,* 1995 EG&G ORTEC Catalog (EG&G ORTEC, 100 Midland Road, Oak Ridge, TN 37830-9913).

Nog91 J. Nogami, A. A. Baski, and C. F. Quate, *Appl. Phys. Lett.* **58**, 475 (1991).

Ohn94 T. Ohno, *Phys. Rev. Lett.* **73**, 460 (1994).

Ost92 H. J. Osten, E. Bugiel, and J. Klatt, *Appl. Phys. Lett.* **61**, 1918 (1992).

Oya95 H. Oyanagi, K. Sakamoto, and R. Shioda, *Phys. Rev.* B **52**, 5824 (1995).

Pap86 L. Papagno, X. Y. Shen, J. Anderson, G. Schirripa Apagnolo, and G. J. Lapeyre, *Phys. Rev.* B **34**, 7188 (1986).

Pat95 L. Patthey, E. L. Bullock, T. Abukawa, S. Kono, and L. S. O. Johansson, *Phys. Rev. Lett.* **75**, 2538 (1995).

Pic73 S. T. Picraux, J. A. Borders, and R. A. Langley, *Thin Solid Films* **19**, 371 (1973).

Pie63	G. R. Piercy, F. Brown, J. A. Davies, and M. McCargo, *Phys. Rev. Lett.* **10**, 399 (1963).
Pre92	H. Presting, H. Kibbel, M. Jaros, R. M. Turton, U. Menczigar, G. Abstreiter, and H. G. Grimmeiss, *Semicond. Sci. Technol.* **7**, 1127 (1992).
Qin96	X. R. Qin and P. R. Norton, *Phys. Rev.* B **53**, 11100 (1996).
Red82	A. Redondo and W. A. Goddard III, *J. Vac. Sci. Technol.* **21**, 344 (1982).
Rei97	D. reinking, M. Kammler, M. Horn-von Hoegen, and K. R. Hofmann, *Appl. Phys. Lett.* **71**, 924 (1997).
Ric90	M. Richter, J. C. Woicik, J. Nogami, P. Pianetta, K. E. Miyano, A. A. Baski, T. Kendelewicz, C. E. Bouldin, W. E. Spicer, C. F. Quate, and I. Lindau, *Phys. Rev. Lett.* **65**, 3417 (1990).
Rob63	M. T. Robinson an O. S. Oen, *Phys. Rev.* **132**, 2385 (1963).
Sak94	A. Sakai and T. Tatsumi, *Appl. Phys. Lett.* **64**, 52 (1994).
Saku76	T. Sakurai and H.D. Hagstrum, *Phys. Rev.* B **14**, 1593 (1976).
Sch90	A. J. Schell-Sorokin and R. M. Tromp, *Phys. Rev. Lett.* **64**, 1039 (1990).
Schl59	R. E. Schlier and H. E. Farnsworth, *J. Chem. Phys.* **30**, 917 (1959).
Sei93	L. E. Seiberling, P. F. Lyman, and M. W. Grant, *J. Vac. Sci. Technol.* A **11**, 715 (1993).
Sho93	F. Shoji, K. Kusumura and K. Oura, *Surf. Sci. Lett.* **280**, L247 (1993).
Sli92	W. F. J. Slijkerman, P. M. Zagwijn, J. F. van der Veen, D. J. Gravesteijn, and G. F. A. van der Walle, *Surf. Sci.* **262**, 25 (1992).
Smu92	P. J. M. Smulders, A. Dygo, and D. O. Boerma, *Nucl. Instrum. Methods* B **67**, 185 (1992).
Sta12	J. Stark, *Phys.* Z. **13**, 973 (1912).
Tan93	S. Tang and A. J. Freeman, *Phys. Rev. B* **47**, 1460 (1993).
Ter94	J. Tersoff, A. W. Denier van der Gon, and R. M. Tromp, *Phys. Rev. Lett.* **72**, 266 (1994).
Tes95	J. R. Tesmer and M. Nastasi (ed.), *Handbook of Modern Ion Beam Materials Analysis* (Materials Research Society, Pittsburgh, PA, 1995).

Tho91 J. M. C. Thorton, A. A. Williams, J. E. MacDonald, R. G. van Silfhout, J. F. van der Veen, M. S. Finney, and C. Norris, *J. Vac. Sci. Technol.* B **9**, 2146 (1991).

Tou93 E. Tournie and K.H. Ploog, *Thin Solid Films* **231**, 43 (1993).

Tro92 R.M. Tromp and M.C. Reuter, *Phys. Rev. Lett.* **68**, 954 (1992).

Voi95 B. Voigtländer, A. Zinner, T. Weber, and H. P. Bonzel, *Phys. Rev.* B **51**, 7583 (1995).

Wam95 W. R. Wampler, *Phys. Rev.* B **51**, 4998 (1995).

Wan93a Y. Wang, M. Shi, and J. W. Rabalais, *Phys. Rev.* B **48**, 1678 (1993).

Wan93b Y. Wang, M. Shi, and J. W. Rabalais, *Phys. Rev.* B **48**, 1689 (1993).

Wol92 R. W. Wolkow, *Phys. Rev. Lett.* **68**, 2636 (1992).

Woo94 D. P. Woodruff and T. A. Delchar, *Modern Techniques of Surface Science* (Cambridge University Press, Cambridge, UK, 1994).

Yu94a B.D. Yu, T. Ide, and A. Oshiyama, *Phys. Rev.* B **50**, 14631 (1994).

Yu94b B.D. Yu and A. Oshiyama, *Phys. Rev. Lett.* **72**, 3190 (1994).

Zan88 A. Zangwill, *Physics at Surfaces* (Cambridge University Press, Cambridge, UK, 1988).

Zhe92 X. M. Zheng and P. V. Smith, *Surf. Sci.* **279**, 127 (1992).

Zie77 J. F. Ziegler, *Helium Stopping Powers and Ranges in All Elemental Matter* (Pergamon, New York, NY 1977).

BIOGRAPHICAL SKETCH

Born in Houston, Texas in 1961, Allison Arthur Bailes III lived the lower middle class, nuclear family life with his parents, Allison Arthur Bailes Jr. and Christine L. Bailes (at the time), and sisters, Ann and Catherine. Living in a brand new, suburban, *Leave It to Beaver* neighborhood, he appeared headed for a life of white middle-class values and relative economic privilege. He built forts with his friends, caught "crawdads" in the bayou, attended Windsor Village Elementary School, learned to ride a bicycle and crash a minibike, was struck by a car while attempting to cross a busy street, and set a field on fire.

He enjoyed visiting his paternal grandparents, Allison Arthur Bailes Sr. and Hazel Green Bailes, in Leesville, Louisiana. They lived in a big, old house on a mostly wooded forty acres, with a large shed and "warehouse" (really a workshop) filled with dust-covered old junk, and they had a large garden. He idolized his grandfather, an electrician and plumber in business for himself (Bailes Electric Co.), and once asked for a "bald-headed haircut just like Pap-paw's" when they went to the barber shop together.

After living with his grandparents in Leesville for most of his fourth grade year, he moved to southern Louisiana with his mother and sisters. Living with the Cajuns of that region, he experienced culture shock and encountered working class values for the first time. As Allison rode his bicycle around the block in his new neighborhood on his first day there, a group of neighborhood kids tried to beat him up. They failed to catch him that time, but that event set the tone for the eight years he spent with the Cajuns. He graduated from South Terrebonne High School in Bourg, Louisiana, in 1979 and has visited the area only once since 1982.

From 1979 to 1983, Allison attended Centenary College of Louisiana in Shreveport. Upon graduating with the Bachelor of Science in physics in 1983, he rode his bicycle from Shreveport to St. Louis, Missouri, and started graduate school in physics at Washington University. Because of a yearning to experience life "on the outside," however, he dropped out of graduate school early in his first semester.

The following year he moved to Oregon and then Washington, where for four years he worked as a telemarketer, an electronics technician, a busboy, and as a residential window cleaner in business for himself. It was in Seattle that he met Myra in 1985. Together they learned to play recorder, hiked in the mountains, read books about education, grew organic vegetables in a community garden, and drove a 1965 VW bus with no clutch from the Grand Canyon to the San Francisco Bay area. Allison and Myra were married in Port Townsend, Washington, in 1988.

He and Myra moved to Leesville, Louisiana, in 1988 to become teachers. Allison taught high school physics, chemistry, physical science, and earth science and sponsored the Science Club at Pickering High School in the 1988-89 school year. Louisiana had not changed much in the five years he had been away, so in August of 1989 Allison and Myra moved to Tarpon Springs, Florida. There Allison taught high school physics, physical science, and earth science from 1989 to 1991 at Tarpon Springs High School (TSHS). Some memorable experiences there include the catapult contest of 1989 and the egg drop of 1990. The most bizarre entries from those events were Ricky Aldape's catapult made of a ruler and an electric pencil sharpener (the ruler broke) and Andy Boeckl's jello-filled soccer ball as egg protection (the egg did not break). In his second year at TSHS, Allison attempted—and failed—to have candy sales banned from campus and also sought—and won—the right of peace groups to have access to students.

Faced with the necessity to take education courses if he wanted to continue teaching, Allison decided instead to return to school full time and pursue the Ph.D. in physics. In the fall of 1991, he returned to graduate school, this time at the University of Florida. After surviving the core courses during the first two years, he passed the comprehensive exams in August 1993 and began working with Professor L. E. Seiberling shortly thereafter. With her, he has studied the structure of adsorbates on the Si(100) surface using the transmission ion channeling technique. He received a Master of Science degree in 1995 and a Master of Science in Teaching degree in 1997. Following graduation from the University of Florida in 1998, Allison appears headed for a suburban, middle-class life and relative economic privilege, at least for a year, as he will be a visiting assistant professor at Haverford College in Pennsylvania in the fall.

I certify that I have read this study and that in my opinion it conforms to acceptable standards of scholarly presentation and is fully adequate, in scope and quality, as a dissertation for the degree of Doctor of Philosophy.

Lucy E. Seiberling, Chairperson
Professor of Physics

I certify that I have read this study and that in my opinion it conforms to acceptable standards of scholarly presentation and is fully adequate, in scope and quality, as a dissertation for the degree of Doctor of Philosophy.

F. Eugene Dunnam
Professor of Physics

I certify that I have read this study and that in my opinion it conforms to acceptable standards of scholarly presentation and is fully adequate, in scope and quality, as a dissertation for the degree of Doctor of Philosophy.

Christopher J. Stanton

Christopher J. Stanton
Professor of Physics

I certify that I have read this study and that in my opinion it conforms to acceptable standards of scholarly presentation and is fully adequate, in scope and quality, as a dissertation for the degree of Doctor of Philosophy.

John M. Graybeal

John M. Graybeal
Associate Professor of Physics

I certify that I have read this study and that in my opinion it conforms to acceptable standards of scholarly presentation and is fully adequate, in scope and quality, as a dissertation for the degree of Doctor of Philosophy.

Gar B. Hoflund

Gar B. Hoflund
Professor of Chemical Engineering

This dissertation was submitted to the Graduate Faculty of the Department of Physics in the College of Liberal Arts and Sciences and to the Graduate School and was accepted as partial fulfillment of the requirements for the degree of Doctor of Philosophy.

August 1998

Dean, Graduate School